Space Sci Rev (2016) 200:495–528
DOI 10.1007/s11214-015-0232-1

The MAVEN Solar Wind Electron Analyzer

D.L. Mitchell[1] · **C. Mazelle**[2,3] · **J.-A. Sauvaud**[2,3] · **J.-J. Thocaven**[2,3] · **J. Rouzaud**[2,3] · **A. Fedorov**[2,3] · **P. Rouger**[2,3] · **D. Toublanc**[2,3] · **E. Taylor**[1] · **D. Gordon**[1] · **M. Robinson**[1] · **S. Heavner**[1] · **P. Turin**[1] · **M. Diaz-Aguado**[1] · **D.W. Curtis**[1] · **R.P. Lin**[1] · **B.M. Jakosky**[4]

Received: 15 December 2015 / Accepted: 24 December 2015 / Published online: 22 February 2016

Abstract The MAVEN Solar Wind Electron Analyzer (SWEA) is a symmetric hemispheric electrostatic analyzer with deflectors that is designed to measure the energy and angular distributions of 3-4600-eV electrons in the Mars environment. This energy range is important for impact ionization of planetary atmospheric species, and encompasses the solar wind core and halo populations, shock-energized electrons, auroral electrons, and ionospheric primary photoelectrons. The instrument is mounted at the end of a 1.5-meter boom to provide a clear field of view that spans nearly 80 % of the sky with ∼20° resolution. With an energy resolution of 17 % ($\Delta E/E$), SWEA readily distinguishes electrons of solar wind and ionospheric origin. Combined with a 2-second measurement cadence and on-board real-time pitch angle mapping, SWEA determines magnetic topology with high (∼8-km) spatial resolution, so that local measurements of the plasma and magnetic field can be placed into global context.

Keywords Mars · Ionosphere · Solar wind · MAVEN mission · Electrostatic analyzer

1 Introduction

The Mars Atmosphere and Volatile Evolution (MAVEN) mission is the first dedicated to studying the structure and variability of Mars' upper atmosphere, the processes that control it, and the importance of atmospheric escape to space today and over the planet's history (Jakosky et al. 2015). The MAVEN orbit has an inclination of 74°, a period of 4.5 hours, an apoapsis distance of 2.8 Mars radii (R_{M}), and a periapsis altitude of ∼150 km, with four

---

Note by the editor: This paper was meant to be part of the topical volume on 'The Mars Atmosphere and Volatile Evolution (MAVEN) Mission', Volume 195, 2015, edited by C.T. Russell and B.M. Jakosky.

✉ D.L. Mitchell
mitchell@ssl.berkeley.edu

1 Space Sciences Laboratory, University of California, Berkeley, USA

2 CNRS, Institut de Recherche en Astrophysique et Planétologie, Toulouse, France

3 University Paul Sabatier, Toulouse, France

4 Laboratory for Atmospheric and Space Physics, University of Colorado, Boulder, USA

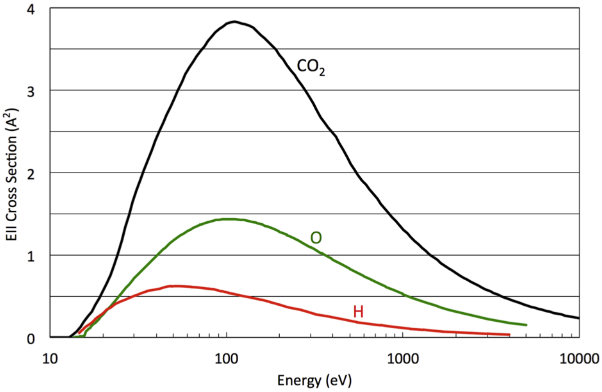

Fig. 1 Cross sections for electron impact ionization of CO_2 (Itikawa 2002), O (Thompson et al. 1995), and H (Shah et al. 1987) based on laboratory measurements

strategically located, week-long “deep dip” campaigns during which periapsis is lowered to ~125 km. Over the course of the one-Earth-year primary mission, the orbit precesses so that the periapsis and apoapsis points visit a wide range of longitudes, latitudes, solar zenith angles, and local times. The MAVEN science payload consists of three components: the Imaging Ultraviolet Spectrograph (IUVS, McClintock et al. 2015), the Neutral Gas and Ion Mass Spectrometer (NGIMS, Mahaffy et al. 2015), and the Particles and Fields Package (PFP), which is a comprehensive suite designed to measure solar ultraviolet, solar wind, and solar storm inputs into the Mars system, the response of the system to variability of these external drivers, and the loss of planetary ions to space. The PFP suite includes two identical magnetometers (MAG, Connerney et al. 2015), a suprathermal and thermal ion composition experiment (STATIC, McFadden et al. 2015), a solar wind ion analyzer (SWIA, Halekas et al. 2015), and an extreme ultraviolet monitor (EUV, Eparvier et al. 2015). The suite also includes three instruments that measure electrons throughout the Mars environment: the Langmuir Probe and Waves (LPW) experiment (Andersson et al. 2015), the Solar Wind Electron Analyzer (SWEA, this paper), and the Solar Energetic Particle (SEP) detector (Larson et al. 2015). LPW measures the temperature and density of thermal ionospheric electrons, which have temperatures (kT_e) ranging from 0.01 to 0.5 eV, as well as electric field waves up to 2 MHz. With an energy range of 3–4600 eV, SWEA measures the energy and angular distributions of solar wind electrons, auroral electrons, and ionospheric primary photoelectrons. SEP measures electrons with energies from ~25 keV to 2 MeV.

SWEA measures energies important for electron impact ionization (EII; Fig. 1). Combining measured electron fluxes with EII cross sections allows one to determine the EII rates in all regions sampled by the spacecraft. Although EII is thought to be a minor contribution to the total ionization rate of Mars’ corona (Chaufray et al. 2007), it is an important process near the magnetic pileup boundary (Crider et al. 2000), resulting in a systematic evolution of the electron energy spectrum as shock energized electrons ionize exospheric neutrals. Electron impact ionization is also significant in the day-side ionosphere (Fox 2004), particularly at altitudes below the main ionospheric peak, where soft X-ray photons produce energetic photoelectrons that cause multiple ionizations before they are thermalized. Radio occultation and radar sounding observations show that Mars’ night-side ionosphere is weak, variable and patchy (Zhang et al. 1990; Gurnett et al. 2008; Duru et al. 2011). At altitudes above ~120 km, transport from the sunlit hemisphere (Uluşen and Linscott 2008; Fränz et al. 2010) and electron impact ionization (Fillingim et al. 2010) are the dominant processes for supporting the night-side ionosphere.

Fig. 2 Electron energy distributions in different regions of the Mars environment measured on Dec. 3, 2014: upstream solar wind (*blue*), sheath (*green*), tail lobe (*black*), and ionosphere (*red*). These spectra are not corrected for the effects of the spacecraft potential, which varies among the different regions

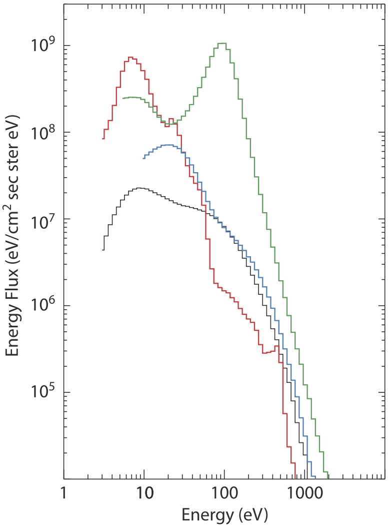

SWEA measures electron pitch angle/energy distributions at high cadence to determine the topology of magnetic fields from both external and crustal sources. In a uniform field, electrons move along helical paths of constant radius and pitch angle, which is the angle between the particle velocity and the magnetic field. The radius of gyration for 100-eV electrons, for example, is typically ∼10 km in the solar wind and less than ∼1 km in crustal magnetic field regions, so electrons are often magnetized, with their centers of gyration constrained to follow the magnetic field line. (Pitch angle scattering can be significant in some regions of the Mars environment, particularly in the sheath with its large magnetic fluctuations and at altitudes below ∼200 km, where electrons scatter from atmospheric species. Drift across magnetic field lines can be significant near strong crustal sources.) Electrons from different regions of the Mars environment can be distinguished by their energy distributions (Mitchell et al. 2001; Fig. 2). Thus, pitch angle resolved energy spectra can be used to determine the plasma source regions sampled by a field line at large distances from the spacecraft, which is a key piece of information for determining magnetic topology and places measurements of the local magnetic field vector into context.

At Mars, where crustal magnetic fields can interact with the interplanetary magnetic field (IMF), pitch angle distributions reveal whether a given field line is connected at both ends to the crust (a closed loop), connected at one end to the crust and one end to the IMF (an open cusp), or connected at both ends to the IMF (Brain et al. 2007). The topology of crustal magnetic fields can significantly influence ionospheric structure. On the day side, closed crustal loops can trap ionospheric plasma, including suprathermal photoelectrons, resulting in enhanced electron temperatures and densities (Krimskii et al. 2003). On the night hemisphere, crustal fields form a pattern of closed crustal loops that can exclude external sources of plasma to form voids (Mitchell et al. 2000). Crustal field lines with a large vertical components tend to connect with draped IMF lines in the tail, providing a conduit for tail plasma to precipitate onto the atmosphere. These open field lines can subsequently close, trapping tail plasma (Ulusen et al. 2011). Ionospheric photoelectrons have been observed up to altitudes of 10,000 km in the tail near the inner magnetospheric boundary (Frahm et al. 2006, 2010), revealing magnetic connectivity to the day-side ionosphere on both draped IMF and crustal magnetic cusps (Liemohn et al. 2006).

On the night hemisphere, electron pitch angle distributions measured at 400 km altitude have been used to map the distribution of open magnetic field lines (Mitchell et al. 2007), revealing the locations of crustal magnetic cusps or field lines draped through the collisional atmosphere. On open field lines, the atmospheric density and magnetic field strength can be probed at altitudes below the spacecraft using the technique of electron reflectometry (Lillis et al. 2008a), which is based on the magnetic mirror effect, or the reflection of charged particles from increasing magnetic field strength. If the field strength (B) increases towards the planet and the fractional change in the field is small over the distance traveled by the electron in one gyration, then the adiabatic approximation holds ($\sin^2\alpha/B = \text{constant}$), and the electron will be reflected back along the lines of force when α reaches 90°. Electrons with pitch angles initially near 90° reflect at high altitudes, while those with smaller pitch angles reflect at lower altitudes. Since the neutral density increases exponentially towards the surface, the probability that an electron will impact a neutral species increases rapidly as the reflection point gets lower. Most electrons that suffer a collision are lost and do not reflect back up to the spacecraft. Thus, the flux of reflected electrons exhibits an attenuation, or "loss cone", that depends sensitively on pitch angle. Measurements of the magnetic field and pitch angle distribution at the spacecraft place a joint constraint on the atmospheric density and magnetic field strength over the altitude range where the loss cone forms (150–250 km). In regions where the crustal field is strong and well constrained by the magnetometer, electron pitch angle distributions can be used to constrain the thermospheric density (Lillis et al. 2008b). In other regions, electron pitch angle distributions can be used to map weak crustal fields at $\sim$170–185 km altitude (Mitchell et al. 2007; Lillis et al. 2008c).

Electron precipitation on these open field lines is highly correlated with enhancements in the night-side ionosphere (Němec et al. 2010; Lillis et al. 2011). Suprathermal electron impact is also responsible for excitation and dissociation of atmospheric species (Fillingim et al. 2010, and references therein), which can lead to detectable auroral emissions (Bertaux et al. 2005) if the precipitating energy flux is high enough (Brain et al. 2006; Dubinin et al. 2008). Energized electron distributions, with 100–2500-eV fluxes enhanced by up to 3–4 orders of magnitude compared to typical distributions, are observed predominantly on open crustal magnetic field lines (Brain et al. 2006; Halekas et al. 2008), suggesting that magnetic reconnection plays a role in accelerating the electron populations and providing access to the atmosphere in cusp regions. Evidence for magnetic reconnection has been observed at 400 km altitude on the Mars night hemisphere (Eastwood et al. 2008).

2 Instrument Description

The Solar Wind Electron Analyzer (SWEA) is a symmetric, hemispheric electrostatic analyzer (Carlson et al. 1983) designed to measure the energy and angular distributions of solar wind electrons and ionospheric photoelectrons in the Mars environment (Fig. 3). The instrument is a collaboration between the Space Sciences Laboratory at the University of California, Berkeley (UCB-SSL) and the Institut de Recherche en Astrophysique et Planétologie (IRAP) in Toulouse, France. SWEA is closely based on an instrument of the same name currently operating on the STEREO spacecraft (Sauvaud et al. 2008). For MAVEN, IRAP provided the analyzer and front-end electronics (microchannel plates, anode, preamplifiers, and high voltage power supply; Fig. 4), while UCB-SSL provided the low voltage power supply and digital electronics (Fig. 5), which controls the analyzer operation and interfaces with the Particles and Fields Data Processing Unit (PFDPU).

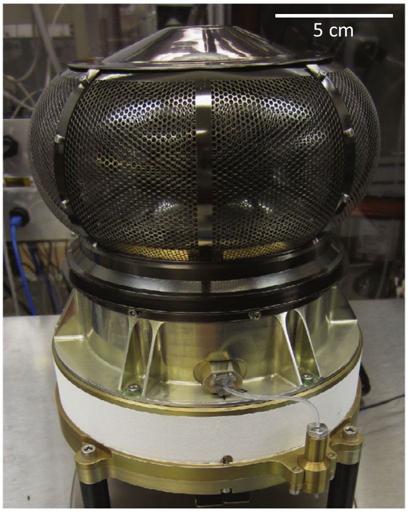

Fig. 3 The MAVEN SWEA instrument (*right*), analyzer cross section (*next page, top*), and electronics block diagram (*next page, bottom*). The *vertical and horizontal dashed lines* in the analyzer cross section are the symmetry axis and aperture center plane, respectively. The electronics independently controls the MCP bias voltage (*MCP HV*) and four sweep voltages: analyzer (V_A), deflector 1 (V_{D1}), deflector 2 (V_{D2}), and V_0

SWEA selects electrons within a specified energy range by placing a potential difference, ΔV_A, between two concentric hemispheres (Fig. 3). Electrons within this energy range are transmitted through the hemispheres to the exit grid (blue trajectories in Fig. 8b), while those outside the range impact the walls and are scattered and absorbed. Only a small fraction of scattered electrons reach the exit grid to be counted. The center energy of transmitted electrons is proportional to ΔV_A, with a constant that depends on the analyzer geometry, and the width of the energy response is proportional to energy ($\Delta E/E = 0.17$). An energy spectrum is obtained by sweeping ΔV_A from 750 to 0.5 V. With a measured analyzer constant of $K_a = 6.17$, this corresponds to an energy range of 4600 to 3 eV.

Electrons transmitted through the analyzer pass through an exit grid and are accelerated by a 300-V potential onto a chevron pair of Photonis microchannel plates (MCPs) that amplify the signal by a factor of $\sim 10^6$. The pre-acceleration potential avoids the sharp decrease in MCP detection efficiency at lower energies (Goruganthu and Wilson 1984). The resulting electron cloud lands on a charge collecting anode that is segmented into 16 equal sized sectors (Fig. 4b). An incident parallel electron beam is focused by the hemispheres to a point on the anode (blue trajectories in Fig. 8b), providing 22.5° azimuth resolution. Charge pulses on each anode sector are detected by one of 16 AMPTEK A111F preamplifiers (Fig. 4c), which provide signals that are counted by a bank of 16-bit counters on the digital electronics board.

The maximum count rate for each sector is limited by the performance of the MCP stack and the preamplifiers. The MCP stack (two 1-mm-thick plates with a pore diameter of 12.5 microns, separated by 30-micron-thick gold spacer rings at the inner and outer edges) supports count rates up to ∼4 MHz with minimal droop, or loss of gain that results when channels have insufficient time to replenish their charge between counts. The A111F preamps have a maximum count rate of ∼2.5 MHz. We define the effective deadtime (τ) for the MCP-anode-preamp chain as the finite time needed to count a single event. During this time the detector is insensitive to any additional events, so the integration time is reduced by the factor $(1 - R'\tau)$, where R' is the measured count rate. We assume that the deadtime is non-paralyzing (independent of count rate) up to some maximum rate that is determined from

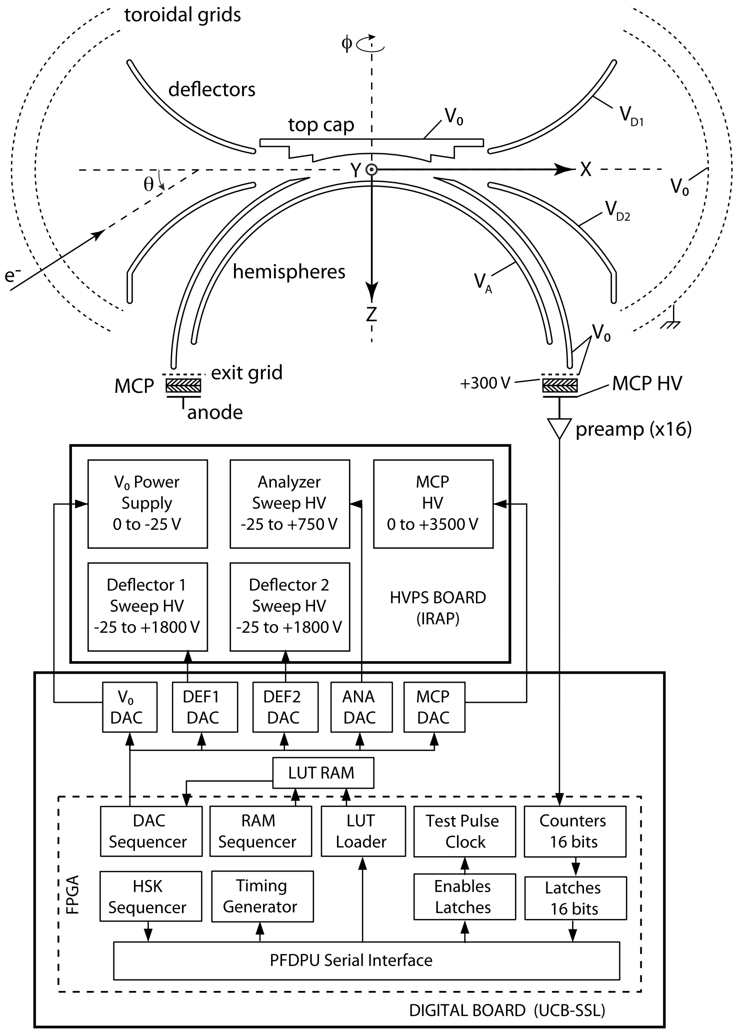

Fig. 3 (*Continued*)

measurement. The true count rate (R) is then:

$$R = R'\left(1 - R'\tau\right)^{-1} \tag{1}$$

With this definition, the deadtime of the MCP-anode-preamp chain was measured to be 2.8×10^{-6} sec. The maximum true count rate per sector that can be reliably corrected for deadtime using Eq. (1) is $\sim 10^6$ s^{-1}. Data are flagged as invalid whenever $R' > 0.75/\tau$. In the Mars environment, the most likely location for this to occur is in the magnetosheath, just downstream of the bow shock, where shock-energized electron fluxes can sometimes saturate the detector from $\sim$50 to $\sim$200 eV.

Electron angular distributions span the full sky, so the field of view (FOV) should be as large as possible to minimize the part of the distribution that is not measured. The field of

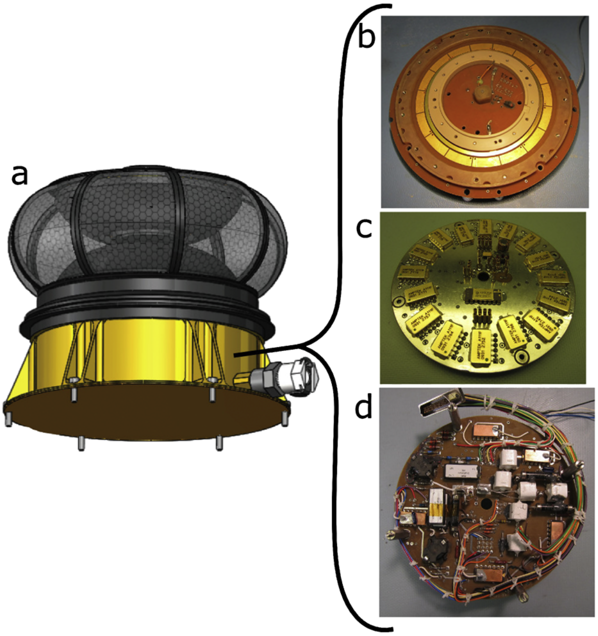

Fig. 4 The SWEA sensor (**a**) and front-end electronics: anode board (**b**), preamplifier board (**c**), and high voltage power supply (**d**). Voltages and signals pass between the boards using pins and sockets. The harness in (**d**) provides the interface between the front-end electronics shown here and the low voltage power supply and digital electronics (Fig. 5). The purge fitting in (**a**) was used to bathe the analyzer and MCPs in dry nitrogen whenever the instrument was not in vacuum. The nitrogen passes via a purge tube through the central holes in the preamplifier and HVPS toward the anode board that holds the MCP detector

view of the concentric hemispheres is 360° × 7°. On a spinning spacecraft, this FOV could be oriented to sweep out the entire sky every half spin; however, MAVEN is a three-axis stabilized spacecraft, so SWEA uses deflectors to sweep the field of view above and below the aperture center plane. Deflection is achieved by placing a potential on either the upper or lower deflector, which bends the electron trajectories through an angle before reaching the aperture center plane and entering the hemispheres (Fig. 8b). The analyzer geometry limits the maximum deflection range to ±60°, outside of which the deflectors themselves begin to impinge on the field of view. The deflection angle depends linearly on the ratio of the deflector voltage to the analyzer voltage (V_D/V_A), so to maintain a constant FOV, deflector voltages must scale with the analyzer voltage. With a maximum deflector voltage of 1800 V, full deflection (±60°) is achieved up to an energy of 2 keV, resulting in an overall FOV of 360° × 120°, which represents 87 % of the sky. At higher energies, the deflection range decreases with energy, reaching ±26° at 4.6 keV.

Electrons entering the aperture pass through two concentric toroidal grids. The outer grid is tied to chassis ground (which is in turn tied to spacecraft ground), while the voltage of the inner grid (V_0) can be commanded between 0 and −25 V. The electrical design is such that the voltages on all surfaces interior to and including the inner toroidal grid (hemispheres, deflectors, top cap, exit grid) are referenced to V_0. In this way, the toroidal grids act as an electrostatic attenuator, decelerating incoming electrons without altering their trajectories or the electrostatic optics interior to the grids.

It is useful to consider an incoming electron's energy at three locations: far from the spacecraft (E), just outside the outer toroidal grid, after it has been accelerated by the potential difference between the spacecraft and the ambient plasma (E'), and just after it has passed through both toroidal grids (E''). One mode of operation scales V_0 to the analyzer voltage:

$$V_0 = \frac{-E''}{2} = \frac{-\Delta V_A K_a}{2} \tag{2}$$

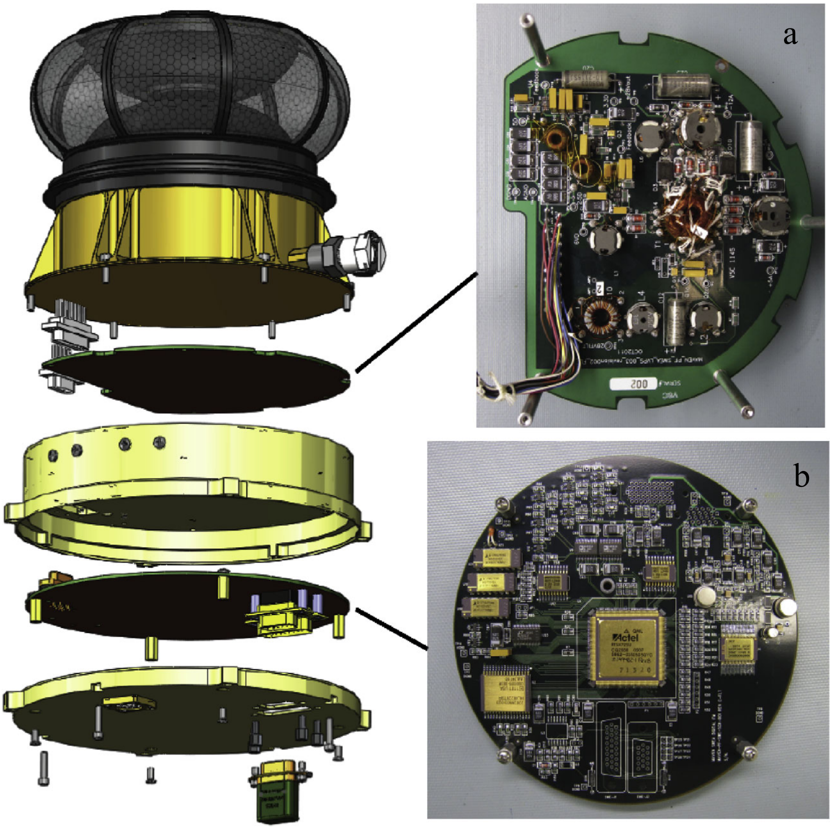

Fig. 5 Exploded view of the pedestal assembly (*left*), with images of the low voltage power supply (*LVPS*), (**a**) and digital board (**b**). The LVPS converts a regulated 28 V provided by the PFDPU to the various voltages required by the digital and front-end electronics. The digital board controls the operation mode and analyzer voltages, accumulates counts from the 16 preamps, monitors instrument voltages and temperatures, and provides a command and data interface with the PFDPU

where ΔV_A is the potential difference between the inner and outer hemispheres, and K_a is the analyzer constant (see Sect. 6.2.3). In this way, the effective energy resolution ($\Delta E/E$, far from the spacecraft) is reduced by the factor $f = 1/(1 + V_0/\Delta V_A K_a) = 2/3$, and the geometric factor is reduced by f^2. This mode is effective up to energies of $E'' = 50$ eV (since the maximum value of V_0 is -25 V), or $E' = 75$ eV just outside the outer grid. At higher analyzer voltages, V_0 is held to its maximum value, so there is no discontinuity in the sweep. This mode can be disabled simply by setting V_0 to zero throughout the sweep. Since finer energy resolution and lower sensitivity are not needed to achieve SWEA's core science goals, we have chosen to disable V_0 for the MAVEN primary mission. However, this functionality can be enabled at any time by uploading a new sweep table that sets V_0 according to Eq. (2). We may enable V_0 in the extended mission for targeted observations where fine energy resolution is advantageous.

There are five key differences between MAVEN SWEA and its predecessor on STEREO. First, the toroidal grids, support ribs, top cover, and deflectors were coated with high-phosphorus, electroless black nickel instead of gold (Fig. 3). Black nickel was chosen because it is conducting, non-magnetic, has a high emissivity (0.4–0.6), and its surface prop-

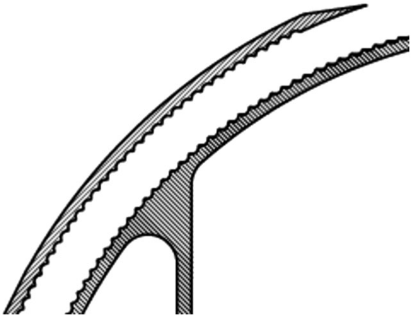

Fig. 6 Detail of the inner and outer hemispheres, showing the scalloping on both surfaces. The scallops, 0.24 mm in depth, suppress scattered and secondary electron contamination. The region between the hemispheres is coated with Cu_2S to suppress scattered photons

erties are not significantly altered by exposure to atomic oxygen, which is present in the Mars environment. The top cap and hemispheres were coated with copper black (Cu_2S), which has a very low UV reflectivity (∼0.01, Zurbuchen et al. 1995) and effectively suppresses photon-induced background whenever sunlight is incident on the SWEA aperture. Coating the top cap with Cu_2S instead of NUFLON avoids the low-energy electron suppression experienced on STEREO SWEA (Fedorov et al. 2011). Second, both the inner and outer hemispheres were scalloped (Fig. 6) to improve scattered and secondary electron suppression by a factor of three compared with STEREO SWEA, for which only the outer hemisphere was scalloped. Third, deflector 1 was moved 0.3 mm toward the top of the analyzer, and deflector 2 was moved 1.0 mm toward the pedestal (both away from the aperture center plane; see Fig. 3) to minimize impingement of the deflectors on the FOV at large deflections. This provides a more uniform sensitivity as a function of deflection angle. Fourth, the high voltage power supply (Fig. 4d) was modified to increase the maximum deflector voltage from 1.5 to 1.8 kV. This allows full ±60° deflections for electrons up to energies of 2 keV. Finally, the number of energy channels was increased from 48 to 64, so that the electron energy distribution can be measured at the analyzer's intrinsic resolution.

The sensitivity is a combination of analyzer geometry, grid transmissions, and MCP efficiency. The analyzer geometric factor can be estimated from simulations, which yield approximately 0.03 cm^2 ster eV/eV. This value does not include grids and posts and assumes a detection efficiency of unity. The toroidal entrance grids have a combined transmission of 0.7, and the exit grid has a transmission of 0.9. There are eight support ribs for the toroidal grids (Fig. 3), each spanning 7° in azimuth at the aperture center plane, resulting in a transmission of 0.8. Thus, grid and post transmissions reduce the simulated sensitivity by a factor of two.

The absolute MCP efficiency is not known accurately, and depends on the bias voltage and the total amount of charge that has been extracted during use. In addition, the relative MCP efficiency for electron detection varies with energy (Goruganthu and Wilson 1984), steeply rising from 0 to 300 eV, then gradually falling by ∼20 % from 300 to 2000 eV. Assuming a nominal efficiency of 0.7 (e.g., McFadden et al. 2008), the simulated sensitivity is further reduced to 0.01 cm^2 ster eV/eV. The geometric factor of the fully assembled analyzer section was measured at IRAP using a calibrated 1.4-keV electron beam and found to be $G = 0.009\ \text{cm}^2\,\text{ster}\,\text{eV/eV}$ for all 16 anodes combined. The measured value, which includes grid transmissions and MCP efficiency, is reasonably close to the expected value, considering the uncertainties. The absolute MCP efficiency is expected to vary with time and will be compensated by monthly or less frequent adjustments to the MCP bias based on in-flight calibrations. The instrument sensitivity will be refined in flight by cross calibration with STATIC, SWIA, and LPW (see Sect. 6.2.3). Table 1 summarizes the instrument parameters.

Table 1 Instrument specifications

Parameter	Value	Comments
$\Delta R/R$	0.072	37.5-mm inner hemisphere radius
Analyzer constant	6.17 eV/V	varies by 1.4 % around azimuth
Analyzer voltage (V_A)	-25 V to 750 V	inner hemisphere voltage
Deflector voltage (V_D)	-25 V to 1800 V	deflectors alternately swept
Offset voltage (V_0)	-25 V to 0 V	interior to toroidal grids
Deflector constant	$10.89° (V_D/V_A)$	from ground calibration
Energy range	3 eV to 4.6 keV	
Analyzer energy resolution	17 % (12 % when V_0 enabled)	$\Delta E/E$, FWHM, measured
Measurement energy resolution	12 %	64-step log energy sweep
Energy sweep rate	64 steps in 1.95 sec	~30 ms per energy step
Deflector sweep rate	28 steps at each energy	~1 ms per deflector step
Azimuth range	360°	16 sectors, each 22.5° wide
Elevation range	±60°	6 bins, each ~20° wide
Instantaneous field of view	360° × 7°	$\theta = 0°$ (no deflection)
Field of view each sweep	360° × 120°	8 % blocked by spacecraft
Analyzer geometric factor	0.01 cm^2 ster eV/eV	simulation with 70 % MCP eff.
	0.009 cm^2 ster eV/eV	ground calibration at 1.4 keV
Measurement cadence	2 sec	1.95 sec meas., 0.05 sec settling
Counter readout	4.35 ms	448 per 1.95 sec

3 Measurement Background and Contamination

Background comes from a variety of sources. The microchannel plates have two principal sources of background: outgassing of adsorbed volatiles from the hygroscopic MgO coating and beta decay of ^{40}K in the MCP glass (Fraser et al. 1987; Siegmund et al. 1988). Outgassing decreases with time during normal instrument operation in vacuum. SWEA operated continuously in interplanetary space from March 19 to July 16, 2014, while the spacecraft was en route to Mars. Measurement of solar wind electrons during this time reduced the outgassing background to a negligible level. Radioactive decay of ^{40}K, with a half-life of $\sim 10^9$ years, is expected to produce a constant background of a few counts per second over the entire detector.

Penetrating particles are another source of background in space (Delory et al. 2012). These come from two sources: galactic cosmic rays (GCRs) and solar energetic particles (SEPs). Protons with energies greater than ~20–40 MeV can penetrate the instrument housing and internal walls to pass through the MCP, where they can trigger electron cascades and generate counts. The GCR energy spectrum peaks near ~1 GeV, at which energy only the planet provides significant shielding. In the MAVEN orbit, shielding from Mars varies from 3 % of the sky at apoapsis to 37 % at periapsis. GCRs are expected to generate several counts per second integrated over the entire detector, modulated by ~35 % over the orbit and by a factor of ~2 over the solar cycle (Bonino et al. 2001). SEP fluxes are episodic and vary widely in intensity, but large events can increase the background by orders of magnitude for days. SEP events also have energetic electron components, with an energy distribution that extends into SWEA's detection range. These can be distinguished from penetrating SEP ions by the variation of count rate with energy (steeply falling for electrons, flat for penetrating ions).

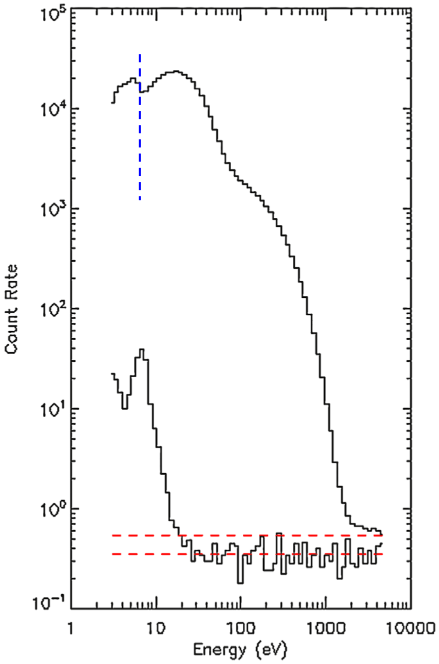

Fig. 7 Measured count rate per anode at 125 km altitude in darkness (*lower spectrum*). The count rate is constant at energies greater than ∼30 eV, revealing the background level per anode (*lower red dashed line*). At higher altitudes (*upper spectrum*), the background is higher because Mars subtends a smaller solid angle and provides less shielding from GCRs (*upper red dashed line*). The integration time is much longer for the upper spectrum, which results in a higher signal-to-noise ratio. The *vertical blue dashed line* is an estimate of the spacecraft potential for the upper spectrum. The spacecraft potential is outside of SWEA's measurement range (<3 V) for the lower spectrum

The background can be measured in flight by selecting a time when the spacecraft is in darkness (to eliminate photon-induced contamination; see below) and by selecting an energy range over which the signal from ambient electrons is negligible. Since the background is independent of the analyzer voltages, it appears as a constant count rate at all energies. This is readily distinguished from the energy spectra of ambient electrons, which typically fall off steeply with energy above ∼100 eV. A suitable location is at an altitude of 125 km on the night hemisphere (Fig. 7), where there is negligible local production (Withers et al. 2008) and external sources of >100-eV electrons are attenuated by interaction with the neutral atmosphere (Lillis et al. 2009). The measured background count rate at this location is 5.6 c/s integrated over the entire detector, with Mars blocking 37 % of the sky. At higher altitudes, the background increases because the planet subtends a smaller solid angle and provides less shielding from GCRs.

When the sensor head is in sunlight, UV photons can enter the aperture, scatter, and produce photoelectrons from interior surfaces. A fraction of these photons scatter down to the MCP, where they produce counts that are independent of the analyzer voltages. Since photons must scatter multiple times to reach the MCP, the use of scalloping and copper black suppresses this contamination to a negligible level, except in rare circumstances, when photons have a direct line of sight to the gap between the hemispheres ($-9° < \theta_{\mathrm{SUN}} < -2°$, see Fig. 8b). In this case, as few as two reflections are needed to reach the MCP, and scattered UV photons increase the total background by about a factor of two, as determined from IRAP ground calibrations.

Photoelectrons emitted from interior surfaces have energies (< ∼60 eV) within the measurement range of the instrument, and if they are directed into the analyzer, can be counted along with ambient electrons at the same energies. Photoelectrons emitted from surfaces closest to the outer hemisphere opening (Fig. 3) have the greatest chance of being transmitted to the MCP. When the top cap is illuminated ($0° < \theta_{\mathrm{SUN}} < 15°$), internal photoelectron

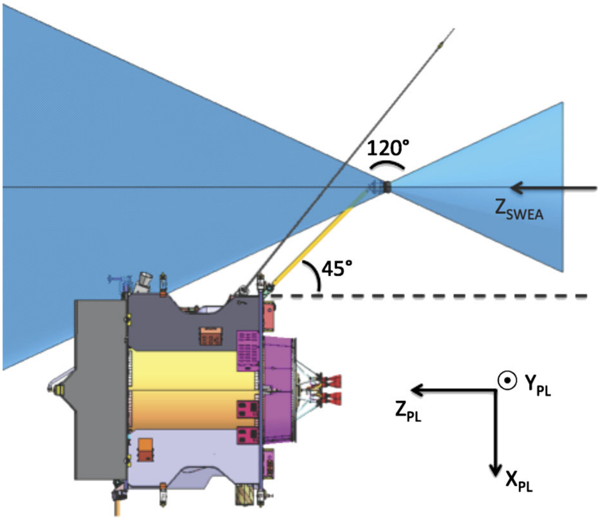

Fig. 8a SWEA is on the end of a 1.5-meter boom, with its symmetry axis (Z_{SWEA}) aligned with the spacecraft Z axis (Z_{PL}). SWEA has a 360° × 120° field of view (blue shading indicates the instrument's blind spots). When the spacecraft Z_{PL} axis points to the Sun, the SWEA electronics box shields the analyzer (including the toroidal entrance grids) from sunlight, thus eliminating photon-induced background inside the instrument

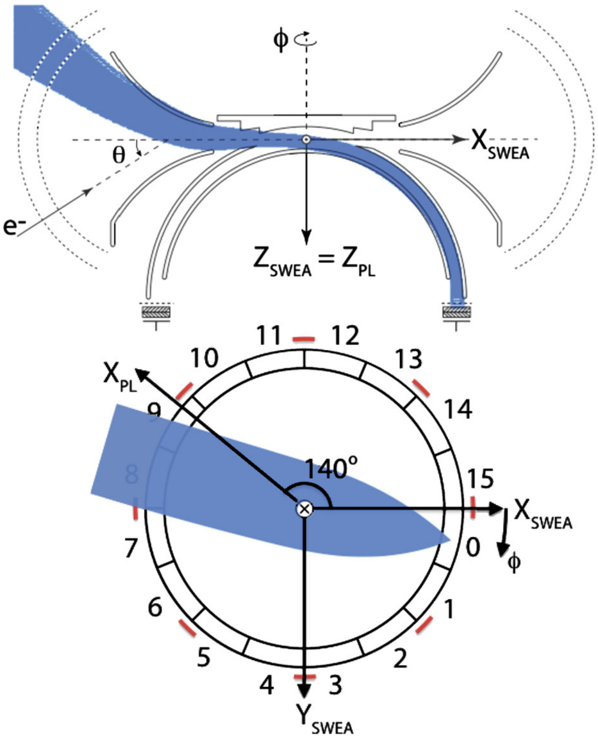

Fig. 8b SWEA coordinates are defined such that the X–Y plane is coincident with the aperture center plane, and the X axis is at the boundary between anodes 15 and 0. Note that Z_{SWEA} is coincident with Z_{PL} and that $+Z$ points from the analyzer to the pedestal. Azimuth (ϕ) and elevation (θ) are defined with respect to SWEA coordinates. *Red segments* indicate the locations of support ribs for the toroidal grids (see also Figs. 1 and 16). Simulated electron trajectories (*blue*) are shown for a deflection of $\theta = -45°$ (see text)

contamination is increased, but this occurs rarely in the MAVEN orbit (see below). Photoelectrons that are not within the angular acceptance range of the analyzer must scatter from internal surfaces and are effectively suppressed by scalloping of the hemispheres.

Scattered and secondary electrons liberated from interior surfaces by impact ionization occur at all times because electrons not transmitted by the analyzer impact interior surfaces

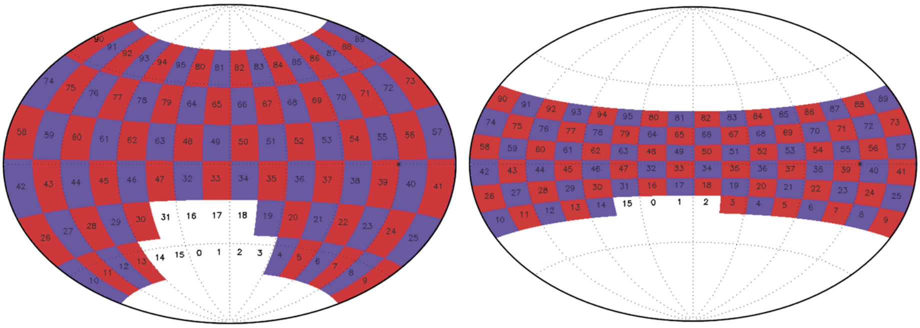

Fig. 9 (*Left*) SWEA's field of view at all energies below 2 keV, mapped in SWEA coordinates over the full sky with an Aitoff projection. The FOV is subdivided into 96 angular bins (16 azimuths × 6 deflections), with a numbering scheme of $i+16j$, where i is the azimuth bin (0–15), and j is the deflection bin (0–5). SWEA's blind spots are two oppositely directed cones, each with a half-width of 30 degrees. Ten of the angular bins, shown in *white*, are blocked by the spacecraft (Fig. 8a). (*Right*) SWEA's field of view at an energy of 4.6 keV. At this energy, four angular bins are blocked by the spacecraft

with sufficient energy to release secondaries. Contamination from scattered and secondary electrons is suppressed by scalloping of the inner and outer hemispheres, and is typically less than a few percent of the signal from ambient electrons.

4 Instrument Accommodation and Spacecraft Environment

SWEA is located at the end of a 1.5-meter boom (Fig. 8a), at which distance the spacecraft blocks 8 % of the instrument's FOV (Fig. 9). As described above, measurement background and contamination depend on the direction of the Sun in SWEA coordinates, which in turn depends on spacecraft orientation. For MAVEN, the spacecraft attitude depends on its location in the orbit, which is divided into four segments: apoapsis, inbound side, periapsis, and outbound side (Jakosky et al. 2015). During the apoapsis and side segments, the spacecraft $+Z_{\mathrm{PL}}$ axis (Fig. 8a) points to the Sun, except twice per week during communication passes, when $+Z_{\mathrm{PL}}$ points to Earth. Whenever $+Z_{\mathrm{PL}}$ points to the Sun, the SWEA sensor head is in the shadow of its own electronics pedestal ($\theta_{\mathrm{SUN}} = 90°$), and there is no photon-induced background produced inside the sensor. Since the maximum elongation of Earth as seen from Mars is 47°, then even during communication passes, $\theta_{\mathrm{SUN}} > 43°$, so that only the toroidal grids and deflectors can be illuminated. Thus, during the apoapsis and side segments, photon-induced background is small or absent.

During the periapsis segment (altitude below ~500 km), the spacecraft is in one of three attitude modes: $+Z_{\mathrm{PL}}$ points to the Sun ("Sun-Velocity" mode), $\pm Y_{\mathrm{PL}}$ points into the ram direction ("Fly-Y" mode), or $-Z_{\mathrm{PL}}$ points into the ram direction ("Fly-Z" mode). In Sun-Velocity mode, there is no photon-induced background. For the other two attitude modes, the elevation of the Sun in SWEA coordinates depends on the orientation of the orbit with respect to the Mars–Sun line. When the orbit plane is nearly coincident with the terminator plane, the Fly-Z attitude places Z_{PL} in the orbit plane, so that the Sun direction is close to the X_{PL}–Y_{PL} plane, and θ_{SUN} is near zero. Similarly, when the orbit plane is nearly coincident with the noon-midnight plane, the Fly-Y attitude places the Sun near the X_{PL}–Y_{PL} plane, and θ_{SUN} is again near zero. In these two cases, the top cap can be illuminated, which increases internal photoelectron background.

As MAVEN orbits Mars, the spacecraft experiences wide range of plasma densities and energy distributions. In addition, ionizing solar UV radiation can be attenuated by the atmosphere or blocked entirely by the planet. The spacecraft responds almost instantly to these different environments by reaching an electrostatic potential such that the net current to the spacecraft is zero. This situation is complicated by the fact that MAVEN has both conducting and insulating surfaces, which can experience different currents and reach different potentials, depending on the orientation of the spacecraft. The largest conducting areas are the spacecraft body (which is covered with grounded, conducting blankets) and the backs of the solar panels. The largest insulating areas are the fronts of the solar panels and the radome covering the high gain antenna (HGA). All conducting areas of the spacecraft have a common ground, to which SWEA is connected. In the following discussion, the "spacecraft potential" (φ) refers to the conducting part of the spacecraft.

In low density environments (anywhere outside the ionosphere) when the spacecraft is in sunlight, the dominant current results from photoelectrons emitted by the spacecraft. This is partially offset by the plasma current (collisions of ions and electrons with the spacecraft), which is negative because of the much larger electron mobility. This causes the spacecraft to charge positive until it reaches a potential sufficient to attract enough photoelectrons back to the spacecraft to achieve zero net current. The magnitude of this potential depends on the flux of ionizing radiation and the local plasma density, as well as the photoemission and secondary emission properties of the spacecraft (Ishisaka et al. 2001). Values upstream of Mars' bow shock and in the magnetosheath, where the ambient density typically exceeds $\sim 1\ \text{cm}^{-3}$, range from a few volts up to $+10$ V. In contrast, the spacecraft charges negative in the planet's shadow, where photoemission is absent, and the plasma current dominates.

In the ionosphere, where the plasma density is orders of magnitude higher, the current resulting from charged particles impacting the spacecraft can be significant compared with the photoelectron current. Near periapsis, ion thermal and bulk velocities are much less than the spacecraft orbital velocity, so the ion current is collimated in the ram direction, whereas much faster moving electrons can reach the spacecraft from all directions. Consequently, the plasma and photoelectron currents to the conducting part of the spacecraft depend on the spacecraft orientation with respect to the ram and sun directions. These directions vary through the mission depending on the periapsis mode (Sun-Velocity, Fly-Y, or Fly-Z) and on the orientation of the orbit with respect to the Mars–Sun line. To date, measured potentials near periapsis range from about -1 to -18 V.

The spacecraft potential affects plasma measurements by shifting the energies of incoming ions and electrons, bending the trajectories of low energy and low mass charged particles, and repelling like-charged particles with energies at or below the potential. At high altitudes in sunlight, MAVEN charges to a positive potential of several volts. Spacecraft photoelectrons with energies below $-q\varphi$, where q is the electron charge, are attracted back to the spacecraft, while those with energies above $-q\varphi$ escape. Meanwhile, ambient electrons are accelerated through the spacecraft potential and shifted in energy. Thus, an instrument mounted on (and at the same potential as) the spacecraft measures spacecraft photoelectrons for $E' < -q\varphi$ and ambient electrons for $E' > -q\varphi$. SWEA's energy range extends down to 3 eV, so that both populations are typically observed in the solar wind and magnetosheath. The boundary between the two populations is often marked by a sharp change or reversal of slope in the energy spectrum at $E' = -q\varphi$ (Figs. 7 and 21). This feature provides a useful estimate of the spacecraft potential, which can be used to transform measured energies and plasma moments from the spacecraft frame to the plasma frame (McFadden et al. 2007). In the ionosphere, discrete features of the primary photoelectron spectrum can also be used to estimate the spacecraft potential (Frahm et al. 2006). On MAVEN, an independent measure of the spacecraft potential is provided by the Langmuir Probe and Waves (LPW) experiment (Andersson et al. 2015).

When the spacecraft charges negative, part of the electron distribution is repelled by the spacecraft or shifted to energies below SWEA's measurement range. In the planet's shadow, electron densities calculated from SWEA measurements can appear smaller than ion densities calculated from STATIC and SWIA measurements, even after correction for spacecraft potential. In the ionosphere, the thermal electron population is cold enough ($kT_e < 0.4$ eV) that it is below SWEA's energy range, even when the spacecraft potential is near zero. In this region, SWEA measures primary photoelectrons produced by ionization of planetary neutrals (mostly CO_2) by solar UV radiation. This non-thermal population represents a small fraction of the total electron density (Mitchell et al. 2000).

5 Instrument Operation

SWEA is controlled by a field-programmable gate array (FPGA), which sets analyzer voltages according to a sweep table, accumulates counts from the 16 preamps, monitors housekeeping values, and provides a command and data interface with the PFDPU. At power on, the PFDPU loads the sweep table into memory on the digital board (Fig. 3), ramps the MCP bias voltage to its operating value, and enables the sweep. During normal operation, the FPGA continuously sends three types of messages to the PFDPU: counter accumulations, housekeeping values, and sweep table checksums. Housekeeping values include analyzer voltages (V_A, V_{D1}, V_{D2}, and V_0—undersampled but with sufficient resolution to verify operation), the MCP bias voltage, and various temperatures and voltages to monitor the environment and operation of the front-end and pedestal electronics. Checksums are provided to verify the integrity of the sweep table, which on rare occasions can be altered by penetrating particles. Two redundant sweep tables are loaded into memory, and if an error is detected in one table, the instrument can be commanded to use to the other. Power cycling refreshes both tables from a copy stored in the PFDPU, which can in turn be refreshed or updated from the ground.

SWEA has a 2-second measurement cycle, which is synchronized to a timing signal provided by the PFDPU. The instrument takes data over the first 1.95 sec, as the analyzer and deflector voltages (V_A, V_{D1}, and V_{D2}) and V_0 are commanded to discrete values according to the sweep pattern shown in Fig. 10. This is followed by a 0.05-sec "gap", during which time the instrument does not take data as the voltages reset and settle in preparation for the next measurement cycle.

The 1.95-sec data collection interval is divided into 1792 equal steps. The analyzer voltage is commanded to 64 logarithmically spaced values from 750 V to 0.5 V, for a duration of 28 steps each. During each analyzer voltage setting, the deflectors are swept in linear ramps that are proportional to the analyzer voltage. This provides a constant angular coverage and resolution as a function of energy until the deflectors reach their maximum potential. To achieve a deflection of 60°, the ratio V_D/V_A must be 5.5. Thus, for a maximum deflector potential of 1800 V (limited by the high voltage power supply), full deflection is achieved up to an analyzer voltage of 327 V, corresponding to an electron energy of 2 keV. At higher analyzer voltages, the deflectors are ramped from 0 to 1800 V to provide the largest FOV possible. The maximum deflection angle is then inversely proportional to energy, falling to 26° at 4.6 keV.

During the first 4 steps of each analyzer setting, the deflector voltages remain constant to allow time for all voltages to settle. (Data collected during these first 4 steps are later

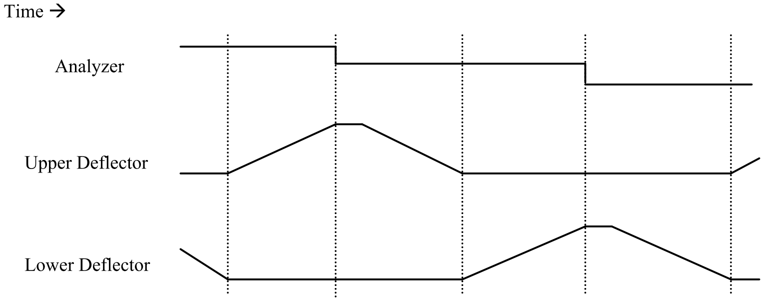

Fig. 10 Sweep pattern schematic for the analyzer and deflector voltages. When enabled, V_0 (not shown) is scaled to the analyzer voltage up to a maximum value of −25 V. *Vertical dotted lines* are at ∼15 millisec intervals. Voltages are not to scale. In particular, the deflector voltage pattern shown in this schematic does not scale with the analyzer voltage as it should

discarded by the PFDPU.) During the next 24 steps, the upper and lower deflectors are alternately ramped, while data are accumulated for each of the 16 anodes in 4-step intervals. This provides six elevation bins with ∼20° elevation resolution (up to 2 keV), which is similar to the 22.5° azimuth resolution and partially compensates for the instrument's intrinsic variable elevation resolution. Above 2 keV, the deflection bin sizes scale with the maximum deflection angle, providing uniform deflection angle coverage as the FOV shrinks. There are a total of $16 \times 6 = 96$ azimuth-elevation bins for each of 64 energy bins.

During each 2-second measurement cycle, the FPGA generates 448 data messages (4-step accumulations of the 1792 data collection steps), with each message consisting of sixteen 16-bit counter values, one for each anode. The accumulation time per anode is $1.95/448 = 4.35$ msec. The PFDPU discards the first of every seven messages that comprise the deflector sweep (to allow for setting time) and organizes the remaining 384 messages into a 64-energy × 16-azimuth × 6-elevation distribution. In order to make best use of SWEA's total telemetry allocation, the PFDPU calculates three data products from this distribution: 3D spectra, pitch angle distributions (PADs), and energy spectra (SPECs). The cadence of each data product is a multiple of 2 sec, which can be set independently of the other data products. All three data products are synchronized, so that each 3D product corresponds precisely to PAD and SPEC data products obtained over the same measurement cycle. This makes it possible to inter-compare the data products, which are summed onboard in different ways and sampled with different cadences.

As it receives SWEA data messages, the PFDPU sorts the data in energy and angle, accumulating counts in 19-bit registers. At the end of each accumulation interval, the 19-bit values are compressed to 8 bits using a scheme that provides 1-count resolution up to 32 counts, 2-count resolution for the next 16 values, 4-count resolution for the next 16, and so on (Table 2).

Raw 19-bit values are rounded down, so each 8-bit value corresponds to a range of possible counts. For example, a telemetry value of 96 decompresses to 512, which corresponds to a range of 512–543 counts. The middle of each range is provided in the SWEA data products, so it is possible to have half counts. The maximum number of counts in this scheme is 524287 ($2^{19} - 1$), which is rounded down to 507904. This 2.5 times larger than needed, even when the instrument is counting at its maximum rate.

Since each telemetry value corresponds to a range of possible raw counter values, this scheme introduces digitization noise. To estimate the contribution from digitization

Table 2 19-to-8 compression

0	1	2	3	4	5	6	7	8	9	10	11	12	13	14	15
16	17	18	19	20	21	22	23	24	25	26	27	28	29	30	31
32	34	36	38	40	42	44	46	48	50	52	54	56	58	60	62
64	68	72	76	80	84	88	92	96	100	104	108	112	116	120	124
128	136	144	152	160	168	176	184	192	200	208	216	224	232	240	248
256	272	288	304	320	336	352	368	384	400	416	432	448	464	480	496
512	544	576	608	640	672	704	736	768	800	832	864	896	928	960	992
1024	1088	1152	1216	1280	1344	1408	1472	1536	1600	1664	1728	1792	1856	1920	1984
2048	2176	2304	2432	2560	2688	2816	2944	3072	3200	3328	3456	3584	3712	3840	3968
4096	4352	4608	4864	5120	5376	5632	5888	6144	6400	6656	6912	7168	7424	7680	7936
8192	8704	9216	9728	10240	10752	11264	11776	12288	12800	13312	13824	14336	14848	15360	15872
16384	17408	18432	19456	20480	21504	22528	23552	24576	25600	26624	27648	28672	29696	30720	31744
32768	34816	36864	38912	40960	43008	45056	47104	49152	51200	53248	55296	57344	59392	61440	63488
65536	69632	73728	77824	81920	86016	90112	94208	98304	102400	106496	110592	114688	118784	122880	126976
131072	139264	147456	155648	163840	172032	180224	188416	196608	204800	212992	221184	229376	237568	245760	253952
262144	278528	294912	311296	327680	344064	360448	376832	393216	409600	425984	442368	458752	475136	491520	507904

noise, we assume that all raw 19-bit counter values over the range of M possible values $(n_1, \ldots, n_M)$ are equally likely. The variance due to digitization, S_D, is then given by:

$$S_\mathrm{D} = \frac{1}{M}\sum_{i=1}^{M}(n_\mathrm{i} - N)^2 = \frac{(M^2 - 1)}{12} \tag{3}$$

where N is the exact mean (mid-point) of the M sequential counter values, n_i. The total variance is $S = N + S_\mathrm{D}$. Using the example above: $N = 527.5$, $M = 32$, $S_\mathrm{D} = 85.25$, and $S = 612.75$. Digitization noise is zero at 1-count resolution ($M = 1$), contributes half of the total variance at $N \sim 4000$, and dominates the variance for $N > 10^5$. The presence of digitization noise means that the relative error, $\sqrt{S}/N$, never falls below ~1 %. In return, compression reduces the telemetry volume by about a factor of two.

6 Calibration

6.1 Detector Simulations

Simulations of the MAVEN SWEA design were performed using software developed at UCB-SSL (McFadden 2007). Simulations are used to optimize the design (such as adjusting the deflector locations) and to evaluate the performance of the instrument in ground testing and in flight. First, a Laplacian solver is used to derive the electrostatic potential when each of the electrically controlled surfaces (hemispheres, deflectors, inner toroidal grid, top cap, and exit grid) in turn is held at unit potential with all other surfaces at ground. The potential is calculated in two dimensions and symmetry is used to determine the potential in three dimensions. Superposition is then used to determine the total potential for any combination of surface potentials. Particles are traced through the electrostatic optics for different combinations of analyzer and deflector voltages to derive the energy and angle response over the FOV. Trajectories are run in reverse, with particles launched from the MCP over a range on initial positions, energies and angles. Trajectories that escape to infinity represent detected particles (Fig. 8b).

6.2 Ground Calibration

The SWEA sensor and front-end electronics (anode, MCP, preamp board, and HVPS) were calibrated at IRAP and then delivered to SSL for integration with the digital electronics and LVPS. IRAP calibrations included deadtime determination, absolute sensitivity calibration, UV contamination test, deflector calibration, and energy–angle response. The last two calibrations were repeated at SSL after integration with the pedestal electronics.

The fully assembled instrument was calibrated at SSL in a vacuum chamber equipped with an electron gun that provided a parallel electron beam over an area larger than SWEA's entrance aperture. The beam energy could be adjusted to span the instrument's full energy range (3 eV to 5 keV). Most calibrations were performed at 1 keV, which allows the deflectors to sweep the FOV over its full range. A set of six Helmholtz coils surrounded the chamber, and the coil currents were adjusted to null the field at the intersection of the electron gun axis and the chamber center line, where the instrument was to be located. With the coil currents constant, the magnetic field was found to vary by ~1 μT from the chamber center line to the wall, a distance of about 30 cm. Beam electrons with energies of 1 keV have gyroradii larger than 75 meters, so deflection of the beam from the electron gun to the

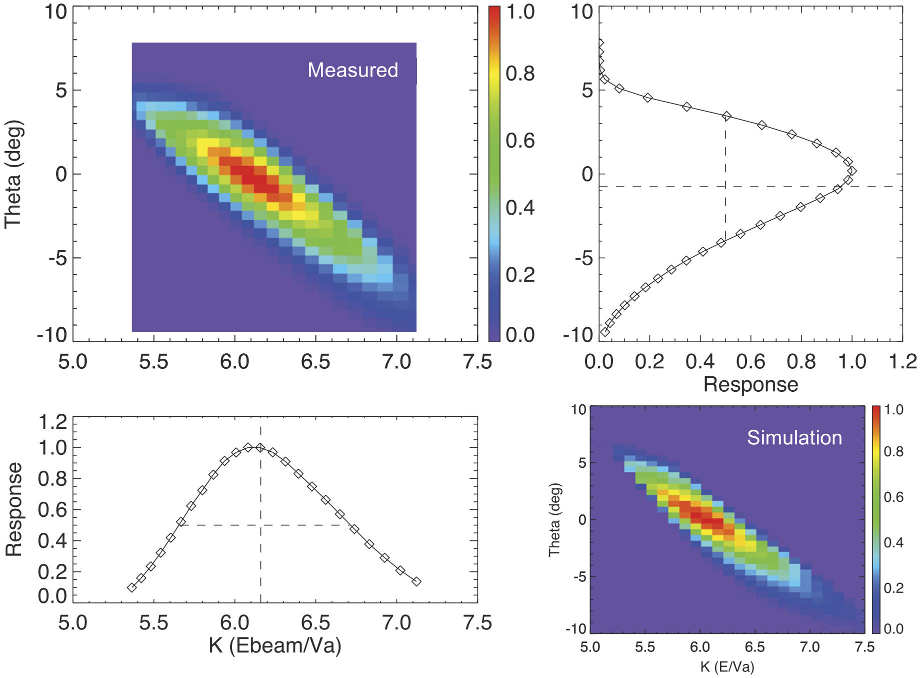

Fig. 11 Measured energy–angle response, normalized to unity, at a mechanical yaw of 0 deg (*top left*). Theta is the deflection angle achieved by varying the deflector voltages (see Fig. 14), and K is ratio of the beam energy (Ebeam) to the analyzer voltage (Va). In this calibration run, the beam energy was held constant while the analyzer voltage was varied. The line drawings are the integrated responses, renormalized to unity, in angle (*upper right*) and energy (*lower left*). The simulation (*lower right*) has been shifted by $\Delta K = -0.44$ (see text)

instrument is less than ~0.2°, and magnetic deflection of electrons within the analyzer is negligible.

The instrument was mounted on a computer controlled mechanical manipulator with three degrees of freedom: (1) roll about the instrument's symmetry axis over >360°, (2) yaw to control the angle between the aperture center plane and the direction of incident electrons from the electron gun, and (3) translation along the chamber center line, to optimize the sensor location with respect to the electron beam.

6.2.1 *Energy–Angle Response*

The instrument energy–angle response was measured for manipulator yaw values ranging from −50° to +60°. (Contact between the harness and the chamber wall prevented more negative yaws.) With the electron beam energy held constant at 1 keV, the analyzer and deflector voltages were varied to map the response function. In Figs. 11, 12 and 13, the measured response is compared with simulations for three sample yaws: 0° and ±45°. Energy is represented as K, which is the ratio of the electron beam energy to the potential difference between the hemispheres (ΔV_A). Deflection angle is a linear function of the ratio of the deflector potential to the analyzer potential (Eq. (4)). This function is calibrated and used to convert V_D/V_A to angle in the measured distributions. In the simulations, angle is determined directly from the particle trajectories.

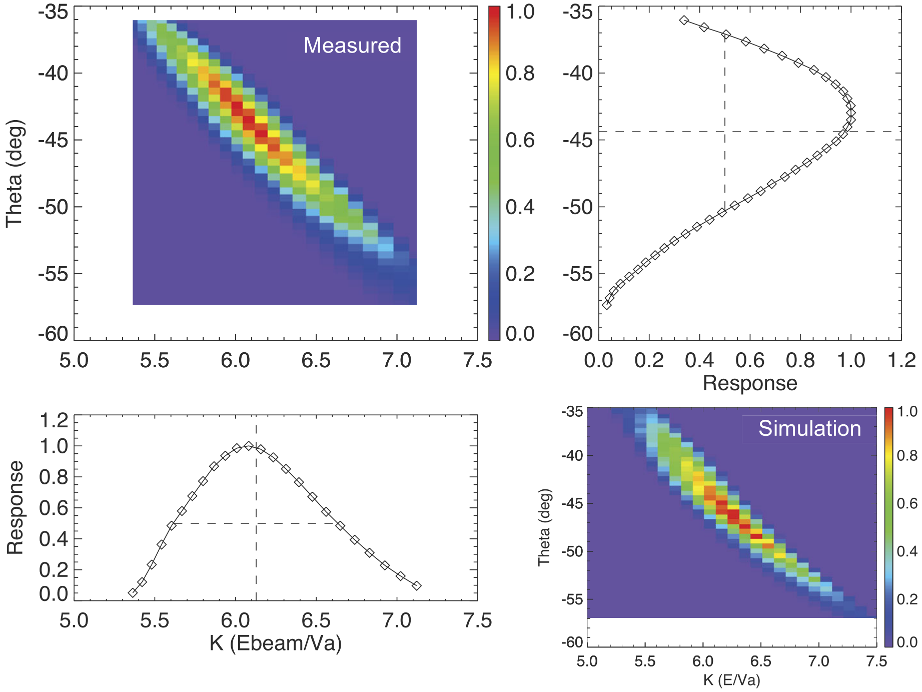

Fig. 12 Measured energy–angle response (*top left* and *both line drawings*) and simulated response (*lower right*) for a yaw of $-45°$. In the simulation, K is shifted by the same amount as for zero yaw. See caption to Fig. 11

In each case, the simulated response must be shifted by $\Delta K = -0.44$ to provide the best agreement with the measured response. This corresponds to a slight increase (∼0.2 mm) in the actual gap between the hemispheres compared with the simulated geometry. This difference can be attributed to two sources. First, the simulated geometry does not include scalloping of the inner and outer hemispheres (Fig. 6). These rounded grooves are 0.24 mm in depth relative to the simulated radii of curvature, so the effective gap is expected to be larger than the simulated gap. Second, the observed variation in K as a function of azimuth (see below), which is a measure of hemisphere concentricity, indicates that mechanical tolerances are of order 0.1 mm. After shifting the simulated energy–angle response, the agreement between measurement and simulation is excellent.

6.2.2 Elevation Response and Deflector Calibration

Measured response functions at manipulator yaws ranging from $-50°$ to $+60°$ were used to determine the relationship between deflection angle and the ratio of the deflector potential (V_D) to the analyzer potential (V_A). Simulations predict that this relationship should be very nearly linear over the full deflection range, until the deflectors themselves begin to impinge on the FOV at the largest deflection angles.

The measurements (upward and downward deflections combined) are well fit with a linear function (Fig. 14):

$$\theta[\mathrm{deg}] = 10.89\left(\frac{V_D}{V_A}\right) - 0.90 \qquad (4)$$

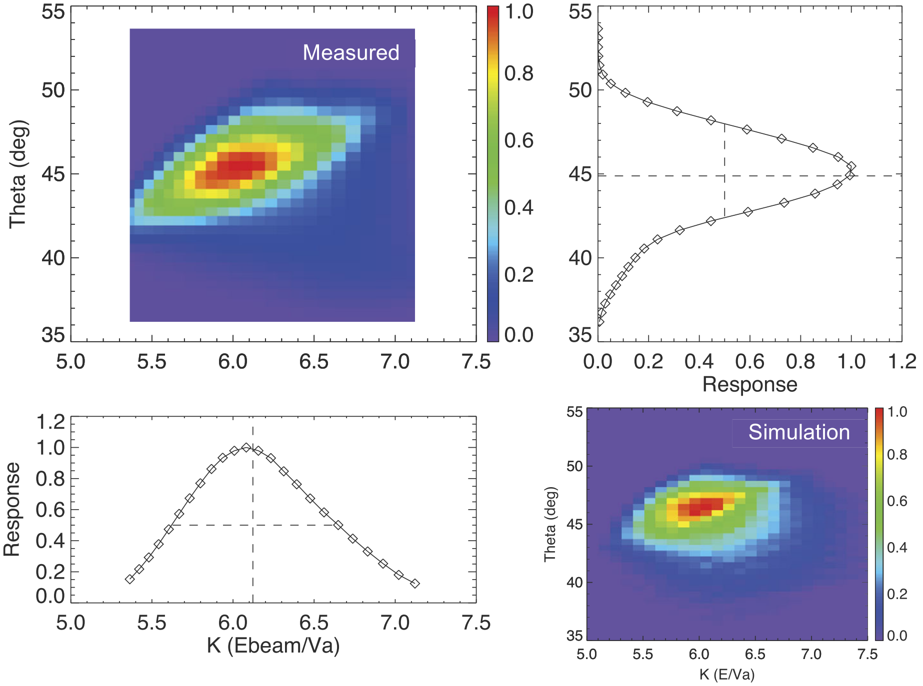

Fig. 13 Measured energy–angle response (*top left* and *both line drawings*) and simulated response (*lower right*) for a yaw of +45°. In the simulation, K is shifted by the same amount as for zero yaw. See caption to Fig. 11

Fig. 14 Mechanical yaw as a function of V_D/V_A. *Diamond symbols* are the measured values, and the *red line* is a linear fit to those measurements. The *blue dashed line* is derived from detector simulations

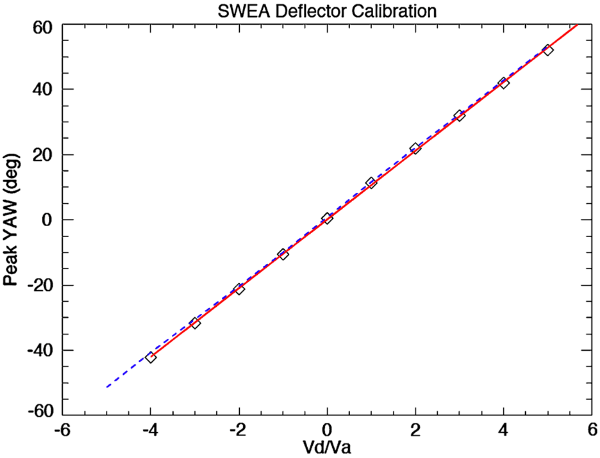

This agrees with simulation to within ∼1°, which is comparable to the accuracy with which the instrument is mounted on the manipulator. The use of deflectors results in a non-uniform angular resolution in elevation (Fig. 15). This is a property of the electrostatic optics, and results from the fact that the electrons can be deflected in the same or opposite sense as the curvature of the trajectory within the hemispheres. A more uniform elevation resolution

Fig. 15 Elevation resolution as a function of elevation. Measured values derived from the energy–angle response (e.g., Figs. 11–13) are shown with symbols. The curve is a polynomial fit to the data. The deflectors are swept with 5° resolution and averaged in groups of four to provide six 20°-wide bins, ranging from −60° to +60°

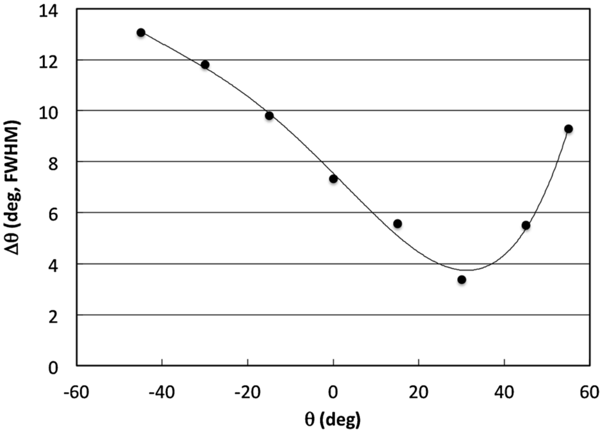

Fig. 16 Energy response obtained by integrating the measured energy–angle response function at a yaw of zero (Fig. 11). The weighted mean value of K and the energy width ($\Delta E/E$, FWHM) are indicated

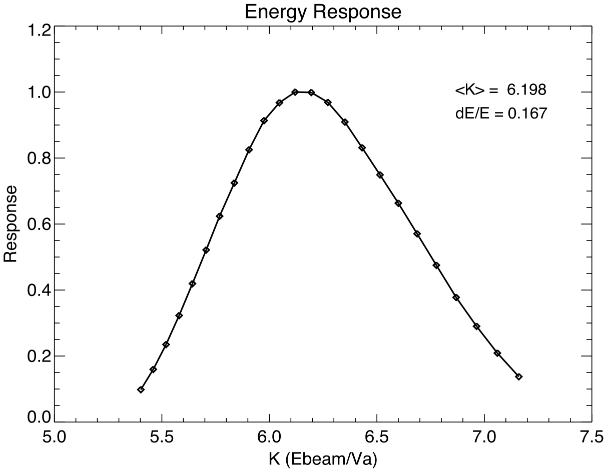

is obtained by averaging over discrete deflector settings, so that the effective resolution is similar to the 22.5° azimuth resolution.

6.2.3 Analyzer Constant and Energy Resolution

The analyzer constant (K_a) is the ratio of the energy of transmitted electrons to the potential difference between the hemispheres (ΔV_A). The beam energy is held constant while the analyzer energy–angle response is measured, as described above. Integrating this distribution over angle provides an energy response function (Fig. 16). The weighted mean value of K for this distribution ($\sum K_i R_i / \sum R_i$, where R is the normalized response) is the analyzer constant, and the full width at half maximum (FWHM) is a measure of the energy resolution.

The analyzer constant measurement was repeated as a function of azimuth by setting manipulator roll to 16 positions around the 360° FOV, all at zero yaw. The results are well fit with a sine function (Fig. 17), which indicates that the most likely cause for the variation is a slight misalignment of the hemispheres. A misalignment of ~0.1 mm would explain the amplitude of the variation. This results in a 1.4 % variation in the energy response around

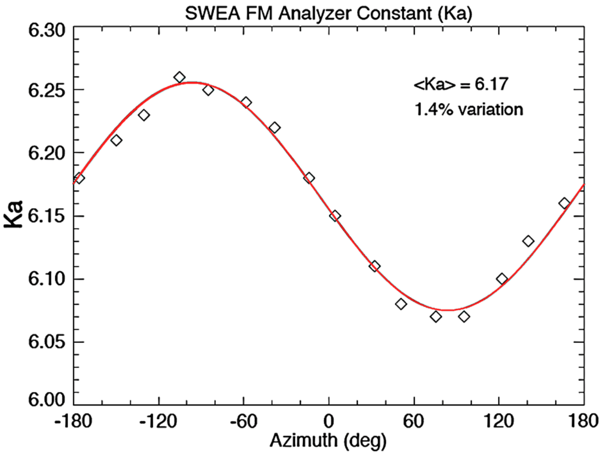

Fig. 17 Analyzer constant (K_a) as a function of azimuth around the FOV. All measurements are at zero elevation. The *red line* is the best-fit sine function

Table 3 Analyzer constant and energy resolution vs. yaw

Yaw	$\langle K \rangle$	$\Delta E/E$ (FWHM)
−45°	6.166	0.160
−30°	6.188	0.169
0°	6.198	0.167
+30°	6.164	0.167
+45°	6.161	0.169
+55°	6.156	0.168

the field of view, which is small compared with the energy resolution ($\Delta E/E$, FWHM) of 17 %.

The analyzer constant and energy resolution do not vary significantly with elevation up to +55°. (The experimental setup at SSL did not permit yaws less then −50°.) Table 3 summarizes results as a function of yaw. The value for yaw = 0 corresponds to Figs. 11 and 16. The total variation of the analyzer constant with elevation is less than 0.5 %, which is three times smaller than the variation with azimuth. There is negligible variation of the energy resolution, except at large negative yaws, which is caused by a slight impingement of the field of view by the deflector.

6.2.4 Azimuthal Response and Field of View

The azimuthal response of the instrument (Fig. 18) was measured by setting the instrument voltages for the center of the response function for a 4 keV beam at yaw = 0 and then rotating the detector at a constant rate about the symmetry axis by 380° (to provide some overlap). As the instrument rotates and collects data, each anode in turn is illuminated by the electron beam. Variations in the response across each anode and the reduction in response at the locations of the support ribs are accentuated by the highly collimated, mono-energetic calibration beam. The 16 sectors provide 22.5° resolution over a 360° range of azimuth. There is no measureable cross talk between the sectors, except for sector 15, which exhibits peak cross talk at the ∼1 % level.

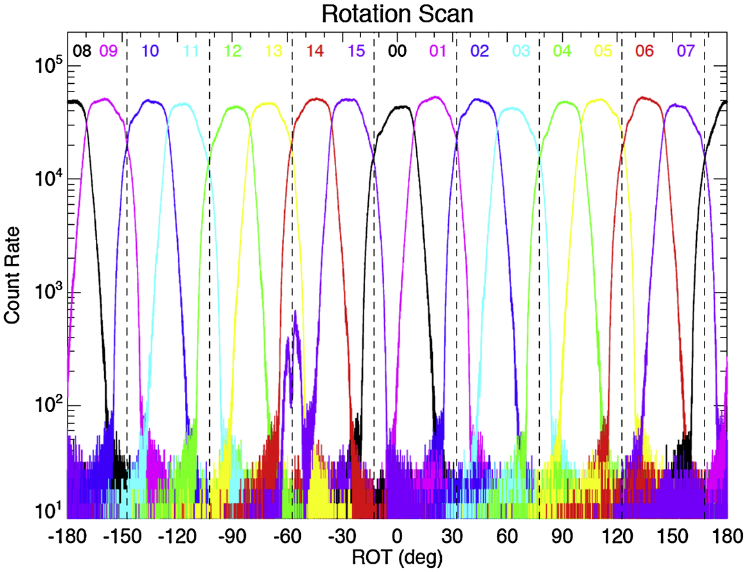

Fig. 18 Detector response as a function of azimuth around the field of view at yaw = 0. The responses of all 16 anodes (numbered 0 through 15) are shown. *Vertical dashed lines* indicate the center locations of support ribs for the toroidal grids. Each rib is 7° wide at zero elevation. Note that the *horizontal axis scale* is manipulator rotation, which is offset by 11.25° from SWEA azimuth (ϕ), as defined in Fig. 8b

6.3 In-flight Calibration

The absolute sensitivity of the instrument depends on the efficiency of the MCPs, which varies with energy and time as charge is extracted during normal operation. To compensate for this gradual reduction in efficiency, monthly calibrations are performed in flight to optimize the MCP bias voltage, which results in discrete jumps in efficiency whenever the bias is increased. Consequently, calibration of the absolute sensitivity must be performed in flight. Since the energy–angle response and accuracy are determined for SWEA, SWIA, and STATIC by calibration on the ground and verification with electrostatic optics simulations, it suffices to use the total plasma density measured by each analyzer as a calibration point to determine the absolute MCP efficiency. Each instrument has a limited energy range and FOV, so care must be taken to ensure that the entire distribution is measured in each case.

The most accurate density determination is provided by LPW, which measures the electron plasma frequency between 90 kHz and 1.67 MHz (Andersson et al. 2015), corresponding to a total plasma density between 100 cm^{-3} and 3×10^4 cm^{-3}. This density range is encountered throughout the upper ionosphere, allowing many measurements of plasma density with an accuracy of ~5 %. The thermal electron population in this region is too cold ($kT_e < 0.4$ eV) to be measured by SWEA, but assuming charge neutrality, the total ion density provides an equally good cross calibration.

Below 250 km altitude, the spacecraft ram velocity (~4 km/s) is larger than the local ion thermal velocity (<1 km/s for O_2^+) and bulk flow velocity (<0.3 km/s; Crowley and Tolson 2007; González-Galindo et al. 2010), so the ion distribution is highly collimated along the ram direction. If the spacecraft potential were zero, the ram velocity would correspond to an energy of 2.8 eV for O_2^+; however, the spacecraft potential in this region is negative (-1 to -18 V, depending on spacecraft orientation), which accelerates ions to ~2–20 eV before they are measured. These energies are below the measurement range of SWIA (Halekas et al. 2015), but well within the range of STATIC (McFadden et al. 2015). With knowledge of the spacecraft potential, the precision of the STATIC density determination is limited only by Poisson statistics, so that the absolute sensitivity of STATIC can be determined from cross calibration with LPW to better than ∼10 %.

As an alternative, we can use START and STOP events in STATIC's time-of-flight section to determine absolute efficiencies for that instrument. The START signal comes from a cloud of electrons that is liberated when an incoming ion passes though the time-of-flight entrance foil, and the STOP signal comes from the ion. The absolute START and STOP efficiencies are determined from ratios of $\mathrm{START}/(\mathrm{START}+\mathrm{STOP})$ and $\mathrm{STOP}/(\mathrm{START}+\mathrm{STOP})$ events, which can be combined with mechanical analyzer geometric factor knowledge from electrostatic optics simulations to get an absolute sensitivity, with error determined by mechanical tolerance and supported by the analyzer energy constant (McFadden et al. 2015). This procedure will work whenever one ion species dominates—for instance in the solar wind or outer magnetosheath. The results of this analysis should agree with cross calibration with LPW, providing a consistency check.

SWIA and STATIC can be calibrated directly to each other in the magnetosheath or in the solar wind at times with less intense fluxes. This calibration can be performed without any requirement for measuring or calculating a total density, since the two sensors have overlap in both energy and angular coverage. Since the two sensors have exactly the same analyzer electrostatic optics, there are very few uncertainties in this calibration. We estimate that this calibration can easily be made to an accuracy of 5 %. Therefore, SWIA can be calibrated to better than 15 % (assuming 10 % accuracy of STATIC calibrations). Finally, SWEA can be calibrated to both SWIA and STATIC in the sheath and/or solar wind. This is a well-understood procedure with extensive heritage from THEMIS (McFadden et al. 2008) and other spacecraft. We estimate that this calibration can be done to 10 % accuracy, ensuring that SWEA can be calibrated to better than 25 %.

The relative sensitivity around the instrument's field of view can also be calibrated in flight using 3D distributions (Sect. 7.1). The technique (Mitchell et al. 2001) takes advantage of the fact that in the plasma rest frame, the electron distribution at a given pitch angle is usually independent of gyration phase around the magnetic field. (Transformation to the plasma rest frame can be accurately performed using SWIA data.) Thus, if two angular bins span the same pitch angle range, they should measure the same electron flux. As the magnetic field direction varies, different pairs of angular bins will span the same pitch angle range, and eventually, all possible pairings occur. The flux ratios of all matched pairs are used to determine the relative sensitivity around the FOV. A particularly useful situation occurs when the magnetic field has an elevation of $\theta = \pm 90^\circ$. In this case, the measured flux should be constant as a function of azimuth. This procedure is over-determined, allowing an estimate of the uncertainty. As the MCP's age, possibly affecting the relative sensitivity around the field of view, this calibration can be repeated.

7 Data Products

7.1 3D Distributions

At the highest resolution, a 3D spectrum consists of 64 energies × 16 azimuths (anode bins) × 6 elevations (deflection bins). The counts in adjacent azimuth bins are summed onboard at the highest positive and negative elevations to reduce the telemetry volume by 17 %

without significantly compromising solid angle resolution. For ease of use in the ground data product, we maintain 16 azimuth bins for all elevations. For the highest positive and negative deflections, we duplicate the summed counts for each pair of azimuth bins and maintain an angular binning factor for subsequently calculating count rate or converting to physical units. (Summing the counts in two adjacent bins effectively doubles the integration time.) The angular binning factor is 2 for the highest positive and negative deflections, and 1 for all other deflections. The distribution can be further summed in groups of 2 or 4 adjacent energy steps. We duplicate summed counts in groups of 2 or 4 in the ground data product, as appropriate, to maintain 64 energy bins. This introduces an energy binning factor, which is used in the same way as the angular binning factor. Finally, the distribution can be sampled every 2^N two-second measurement cycles, where N is an integer ($N \geq 0$), thus reducing the telemetry volume by the same factor. (We sample in time instead of sum over time onboard, since variations in the magnetic field can be significant over the sample interval.) Raw decompressed counts and binning factors are provided in the 3D data products to allow calculation of statistical uncertainties; however, care must be taken, since duplicated bins are not independent.

The 3D product provides the most information, but with a low cadence (16 or 32 sec, depending on altitude, 8 sec for burst) because of the amount of telemetry it consumes. To reduce the total data volume, the PAD and SPEC products are extracted from the 3D product onboard by sampling and/or averaging. All three data products are synchronized, so the 3D product can be used to verify the other two. The 3D data product can be compared with the SPEC data product by summing over the 96 solid angle bins, each weighted by solid angle, and then dividing by the total solid angle subtended by the FOV, thus maintaining units of $\text{eV/cm}^2\,\text{sec}\,\text{ster}\,\text{eV}$. In addition, 3D distributions can be used to investigate the effects of the spacecraft environment on the measurements. For example, the spacecraft photoelectron population can be imaged at energies below the spacecraft potential. This distribution is anisotropic and depends on the illumination pattern of the spacecraft.

Figure 19 shows an example of the 3D data product, summed over a 6.4-minute interval during which the magnetic field direction was nearly constant. This distribution was measured in the solar wind, upstream of the Mars bow shock, at an altitude of 6120 km (2.8 R_M). At an energy of 125 eV (shown here), the distribution is dominated by the solar wind halo population, which is typically beamed away from the Sun along the interplanetary magnetic field. This beam can be seen clearly in the angular distribution centered on the $-\mathbf{B}$ direction, which is determined from fully calibrated Level 2 Magnetometer (MAG) data (Connerney et al. 2015). Ten of the 96 solid angle bins are masked because of spacecraft blockage. Since the spacecraft is fixed in SWEA's field of view, the same bins (0–3, 14–18, and 31) are always marked as invalid in the 3D data product. Figure 19 represents only one of the 32 (binned) energy channels that make up this 3D data product.

7.2 Pitch Angle Distributions

The most scientifically relevant way to organize the electron angular distribution is with respect to the magnetic field. With knowledge of the magnetic field vector measured onboard, the FOV can be mapped into pitch angle (α), which is the angle between an electron's instantaneous velocity vector and the magnetic field:

$$\cos(\alpha) = \cos(\phi - \phi_B)\cos(\theta_B) + \sin(\theta)\sin(\theta_B) \tag{5}$$

where ϕ and θ are the azimuth and elevation of the incident electron, and ϕ_B and θ_B are the azimuth and elevation of the magnetic field vector. The mapping of pitch angle around the field of view varies with time as the magnetic field direction changes.

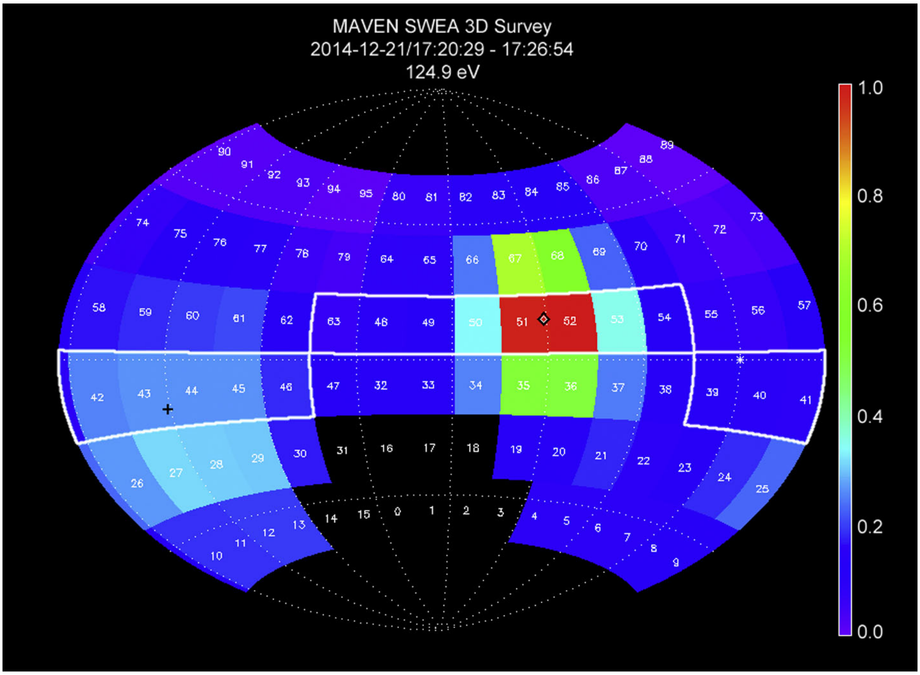

Fig. 19 SWEA 3D data product showing the angular distribution of 125-eV electrons in the solar wind. The data are normalized to unity at the peak energy flux, and relative variations are shown with a linear *color scale*. The data are mapped in SWEA coordinates over the full sky with an Aitoff projection, and each azimuth-elevation bin is labeled with its bin number (0–95). The instrument's blind spots (|elevation| > 60°) and bins blocked by the spacecraft have no color. The magnetic field direction is indicated by the plus (+**B**) and diamond (−**B**) symbols. The sixteen 3D angular bins that make up the PAD distribution for this time are outlined *in white*

Pitch angle distributions (PADs) are generated onboard by flight software in the PFDPU. The first step is to perform a basic calibration of the magnetic field vector (fixed offsets and gains only) and then rotate the vector into SWEA instrument coordinates, so that the 96 solid angle bins can be mapped into pitch angle. Magnetic field data are averaged over the second half of SWEA's 2-sec measurement cycle, during which time the instrument is measuring electrons with energies from 110 to 3 eV. The pitch angle distribution that is placed in telemetry is composed of 16 values: one for each of the 16 azimuth sectors. Flight software determines the optimal deflection bin for each azimuth sector that maximizes the total pitch angle coverage. The solution is a great circle entirely within the FOV that contains the magnetic field vector, or comes as close a possible to doing so. This guarantees that a complete pitch angle distribution is obtained whenever the magnetic field vector is within the FOV, and that any gaps are not larger than the instrument's intrinsic blind spots ($|\theta| > 60°$). The PAD data files contain the magnetic field azimuth and elevation (ϕ_B and θ_B, in instrument coordinates) used by flight software to perform this calculation. Spacecraft blockage is not masked onboard, but affected bins are identified on the ground and marked as invalid. Note that pitch angle distributions are more likely to have reduced coverage as the instrument's FOV shrinks at energies above 2 keV. The algorithm for optimizing the pitch angle coverage of the PAD data product was designed for the full ±60° deflection range, and is less effective for smaller deflection ranges.

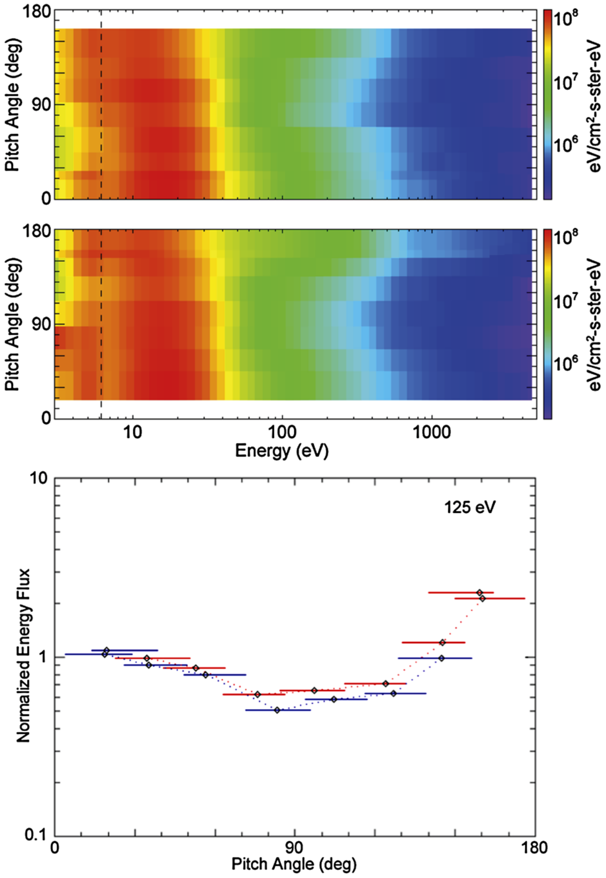

Fig. 20 (*Top*) Electron energy-pitch angle distribution measured in the solar wind over the same time interval in Fig. 19. The pitch angle distribution is measured twice, with anode bins 0–7 above and 8–15 below. An estimate of the spacecraft potential is shown by the vertical *dashed line* (see Fig. 21). (*Bottom*) Pitch angle distribution at 125 eV, with anode bins 0–7 in *blue* and 8–15 *in red*. The mean pitch angle is shown by the *symbol* and the pitch angle range is indicated by the *horizontal bar*. This cut through the 3D distribution (white outline in Fig. 19) does not intersect the spacecraft, so all 16 pitch angle bins represent valid measurements. When a cut does include bins that are blocked by the spacecraft, those bins are flagged as invalid

Figure 20 shows an electron pitch angle distribution measured over the same time interval as the 3D distribution in Fig. 19. The field-aligned beam appears in the pitch angle distribution as an increased flux from ∼135 to 180 degrees. Since the sixteen PAD bins span 360° in azimuth, there is two-fold redundancy. That is, the pitch angle distribution is measured twice, once for each half of the detector. This redundancy can be used to monitor the calibration in fight (under the assumption of gyrotropy). Solid angle bins are ∼20° across, so the basic magnetic field calibration performed onboard is sufficient to optimize the pitch angle coverage provided by this data product. No information is lost in producing a PAD onboard, since it is obtained without averaging in angle. There is a one-to-one mapping between pitch angle bins in the PAD data and solid angle bins in the 3D data (white outline in Fig. 19). To produce calibrated Level 2 PAD data, the pitch angle mapping is refined on the ground using fully calibrated L2 MAG data. In this case, we average the magnetic field over SWEA's 2-sec measurement cycle. The average pitch angle and the range of pitch angles spanned by each bin is provided in the PAD data product.

PADs can be summed onboard in groups of 2 or 4 adjacent energy steps. As before, we duplicate summed counts and record energy binning factors, as appropriate, to maintain 64 energy bins in the ground data product. The PADs can also be sampled every 2^N two-second measurement cycles, thus reducing the telemetry volume by the product of N and the energy binning factor. The PAD energy binning and time sampling can be different from those used in the 3D data product. Raw decompressed counts and binning factors are provided in the PAD data products to allow calculation of statistical uncertainties.

7.3 Energy Spectra

Energy spectra are obtained by taking a weighted average of all 96 azimuth-elevation bins. Before summing, the counts are multiplied by $\cos(\theta)$ to account for variation of the solid angle spanned by each bin:

$$\Delta\Omega = 2\Delta\phi \sin\left(\frac{\Delta\theta}{2}\right)\cos\theta \tag{6}$$

where $\Delta\phi$ and $\Delta\theta$ are the angular bin widths in azimuth (22.5°) and elevation (20°), and θ is the center elevation. To within a constant scaling factor, this weighted summation over angular bins approximates the angular summation of a density moment calculation (Eq. (7)). The on-board angular summation includes ten bins that are blocked by the spacecraft (Fig. 9); however, the SPEC data can be corrected on the ground by comparison with the 3D data, to which proper masking can be applied. The energy summation of the moment calculation can be performed on the ground, or the energy spectrum can be fit with a model to estimate density and temperature. In both cases, a correction for spacecraft potential should be applied.

A weighting factor is provided in the SPEC data product to allow conversion of weighted counts to mean raw count rate per anode, which allows an estimate of deadtime for the summed data. The 3D data can be used to evaluate the accuracy of this estimate, albeit at a lower cadence. Energy spectra always contain all 64 energy steps to provide the best possible energy resolution, and they can be either sampled or summed over every 2^N two-second measurement cycles.

Figure 21 shows an electron energy distribution obtained over the same time interval as in Figs. 19 and 20. The spacecraft potential (+6.2 volts, vertical dashed line) can often be identified by a sharp break in the energy distribution. At energies below this potential, SWEA measures spacecraft photoelectrons that have insufficient energy to escape, and are thus attracted back to the spacecraft. At higher energies, SWEA measures ambient solar wind electrons, shifted in energy by the amount of the spacecraft potential.

Removal of spacecraft photoelectrons and correction for spacecraft potential are critical for estimating density and temperature from the measured electron distributions (McFadden et al. 2007). For example, to estimate electron number density (n_e) from the measured energy flux, we sum over energy and angle:

$$n_e = \left(\frac{m_e}{2}\right)^{1/2} \sum_{\Omega'} \sum_{E'>\varphi} \left(1 - \varphi/E'\right)^{1/2} \left(E'\right)^{-3/2} F'\left(E', \Omega'\right) \Delta E' \Delta\Omega' \tag{7}$$

where E', F', and Ω' are the energy, energy flux, and solid angle as measured in the instrument frame (for SWEA, just outside the outer toroidal grid); $\Delta\Omega'$ is the solid angle spanned by each angular bin (Eq. (6)); φ is the spacecraft potential, and m_e is the electron mass. For the SPEC data product, the summation over angle is performed onboard with $\cos(\theta)$ weighting factors, as described above. For the 3D data product, angular summation is performed on the ground. In this case, further corrections can be made for plasma bulk flow velocity relative to the spacecraft.

The summation over energy is carried out only over energy channels above the spacecraft potential. Since SWEA does not measure the distribution over the full sky, this sum is

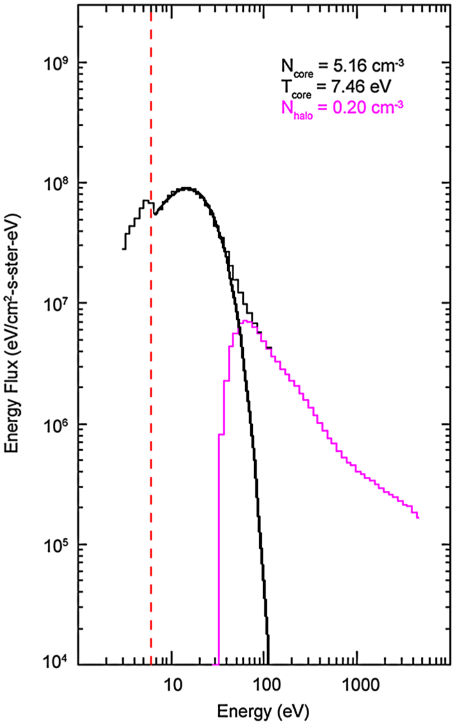

Fig. 21 Electron energy distribution measured at the same time as the 3D and PAD distributions (Figs. 19 and 20). The distribution is calculated onboard by summing the 96 angular bins, weighted by $\cos(\theta)$, for each energy in the 3D distribution. An estimate of the spacecraft potential (6.2 V), determined from the sharp change in slope, is shown by the *dashed red line*. The population below 6.2 eV is spacecraft photoelectrons. The distribution from 6.2 to 30 eV is fit with a Maxwell–Boltzmann distribution ($kT = 7.46$ eV, $N = 5.16$ cm^{-3}, *thick curve*). The residual above 30 eV (*purple histogram*) is the halo population. The background level is $\sim 10^3$ in energy flux units

multiplied by a correction factor $(4\pi / \sum \Delta\Omega')$ to account for the part of the distribution that is not measured, under the assumption that the distribution in the instrument's blind spots is not very different from the part of the distribution that is measured. This can be significantly in error when the magnetic field direction is in one of SWEA's blind spots or is blocked by the spacecraft.

7.4 Data Collection Modes

The instrument has one operational mode, which produces 448 messages synchronized to the sweep pattern every 2-second measurement cycle. Energy averaging and time sampling are performed in the PFDPU when calculating the three SWEA data products. Energy sampling for 3D and PAD products and time sampling for all three products are parameterized and can be adjusted by command to manage SWEA's data production rate. Thus, as the overall telemetry bandwidth varies during the mission (because of the changing Earth-Mars distance), SWEA's data production can vary accordingly.

The energy and time sampling parameters are used to define two data collection modes: solar wind mode and ionosphere mode (Table 4). Solar wind mode is used at high altitudes, where high resolution is less important. This allows us to expend a greater fraction of SWEA's total telemetry allocation to achieve higher resolution at low altitudes. The transition altitude between these two modes is adjustable on the ground. It has been 2000 km since the start of science operations in November 2014 to present.

Each data collection mode produces two data streams: survey and burst. The survey stream provides sufficient resolution to achieve SWEA's scientific goals, and is placed into telemetry in its entirety. The burst stream contains higher energy and/or time resolution

Table 4 SWEA data collection modes

Data type	Mode	Data stream	Energy bins	Cadence (sec)
3D	Ionosphere	Survey	32	16
PAD	(<2000 km)		32	2
SPEC			64	2
3D		Burst	64	8
PAD			64	2
SPEC			–	–
3D	Solar Wind	Survey	32	32
PAD	(>2000 km)		32	4
SPEC			64	4
3D		Burst	32	8
PAD			–	–
SPEC			–	–

and is stored in flash memory within the PFDPU. Only a fraction of the burst data can be telemetered to the ground. Telemetry bandwidth for sending burst data is obtained by lossless compression of the survey data stream. Typically a factor of $\sim$2.5 compression is achieved, which provides space for $\sim$40 % of the burst data. There are 8 GB of burst memory, which is sufficient to store about 28 days of burst data. At each contact (typically twice per week), survey data are reviewed and time ranges of interest are selected. Commands are then sent to the PFDPU at the next contact to downlink the burst data covering the desired time range(s). The burst data have the same format as the survey data. The only differences are the energy and/or time resolutions.

8 Summary

The Solar Wind Electron Analyzer is a symmetric hemispheric electrostatic analyzer with deflectors that is well suited to measuring the energy and angular distributions of solar wind electrons and ionospheric photoelectrons in the Mars environment. SWEA provides three data products: 3D (energy-azimuth-elevation) distributions, pitch angle distributions (2D cuts through the 3D distributions), and energy spectra (integrated over angle). Pitch angle distributions are determined on-board in real time using Magnetometer data. This approach allows complete or nearly complete pitch angle coverage with a cadence (2 sec, $\sim$8 km) sufficient to resolve crustal magnetic cusps, while minimizing SWEA's data volume. The instrument's energy range (3–4600 eV) spans the region where the electron impact ionization cross sections of planetary species are significant, providing key information for constraining ionization and loss of planetary species at high altitude, as well as the ionization and excitation of Mars' upper atmosphere through electron precipitation. SWEA's large field of view, high sensitivity and high measurement cadence provide pitch-angle-resolved energy distributions that identify the plasma source region(s) sampled by a given field line, thus revealing magnetic topology and providing the context necessary to relate local measurements of the plasma and magnetic field to global scales.

Acknowledgements The fabrication, testing, calibration, and operation of MAVEN SWEA has been supported in the United States by the NASA Mars Scout Program and in France by CNES. The authors thank the engineering and technical staffs at SSL and IRAP for their expertise, dedication, and hard work throughout the development of SWEA.

References

L. Andersson, R.E. Ergun, G.T. Delory, A. Eriksson, J. Westfall, H. Reed, J. McCauly, D. Summers, D. Meyers, Space Sci. Rev. **195**(1), 173–198 (2015)

J.-L. Bertaux, F. Leblanc, O. Witasse, E. Quemerais, J. Lilensten, S.A. Stern, B. Sandel, O. Korablev, Nature **435**, 790–794 (2005)

G. Bonino, G.C. Castagnoli, D. Cane, C. Taricco, N. Bhandari, in *Proc. ICRC 2001* (2001), pp. 3769–3772

D.A. Brain, J.S. Halekas, L.M. Peticolas, R.P. Lin, J.G. Luhmann, D.L. Mitchell, G.T. Delory, S.W. Bougher, M.H. Acuña, H. Rème, Geophys. Res. Lett. **33**, L01201 (2006). doi:10.1029/2005GL024782

D.A. Brain, R.J. Lillis, D.L. Mitchell, J.S. Halekas, R.P. Lin, J. Geophys. Res. **112**, A09201 (2007). doi:10.1029/2007JA012435

C.W. Carlson, D.W. Curtis, G. Paschmann, W. Michael, Adv. Space Res. **2**, 67–70 (1983)

J.Y. Chaufray, R. Modolo, F. Leblanc, G. Chanteur, R.E. Johnson, J.G. Luhmann, J. Geophys. Res. **112**, E09009 (2007). doi:10.1029/2007JE002915

J.E.P. Connerney, J. Espley, P. Lawton, S. Murphy, J. Odom, R. Oliversen, D. Sheppard, Space Sci. Rev. **195**(1), 257–291 (2015)

D. Crider, P. Cloutier, C. Law, P. Walker, Y. Chen, M. Acuña, J. Connerney, D. Mitchell, R. Lin, K. Anderson, C. Carlson, J. McFadden, H. Rème, C. Mazelle, C. d'Uston, J. Sauvaud, D. Vignes, D. Brain, N. Ness, Geophys. Res. Lett. **27**(1), 45–48 (2000)

G. Crowley, R.H. Tolson, J. Spacecr. Rockets **44**(6), 1188–1194 (2007)

G.T. Delory, J.G. Luhmann, D. Brain, R.J. Lillis, D.L. Mitchell, R.A. Mewaldt, T. Vilstrup Falkenberg, Space Weather **10**, S06003 (2012). doi:10.1029/2012SW000781

E. Dubinin, M. Fraenz, J. Woch, J.D. Winningham, R. Frahm, R. Lundin, S. Barabash, Planet. Space Sci. **56**, 846–851 (2008)

F. Duru, D.A. Gurnett, D.D. Morgan, J.D. Winningham, R.A. Frahm, A.F. Nagy, J. Geophys. Res. **116**, A10316 (2011). doi:10.1029/2011JA016835

J.P. Eastwood, D.A. Brain, J.S. Halekas, J.F. Drake, T.D. Phan, M. Øieroset, D.L. Mitchell, R.P. Lin, M. Acuña, Geophys. Res. Lett. **35**, L02106 (2008). doi:10.1029/2007GL032289

F.G. Eparvier, P.C. Chamberlin, T.N. Woods, E.M.B. Thiemann, Space Sci. Rev. **195**(1), 293–301 (2015)

A. Fedorov, A. Opitz, J.-A. Sauvaud, J.G. Luhmann, D.W. Curtis, D.E. Larson, Space Sci. Rev. **161**, 49–62 (2011)

J.L. Fox, J. Geophys. Res. **109**, A11310 (2004). doi:10.1029/2004JA010380

M.O. Fillingim, L.M. Peticolas, R.J. Lillis, D.A. Brain, J.S. Halekas, D. Lummerzheim, S.W. Bougher, Icarus **206**, 112–119 (2010)

R.A. Frahm, J.D. Winningham, J.R. Sharber, J.R. Scherrer, S.J. Jeffers, A.J. Coates, D.R. Linder, D.O. Kataria, R. Lundin, S. Barabash, M. Holmström, H. Andersson, M. Yamauchi, A. Grigoriev, E. Kallio, T. Säles, P. Riihelä, W. Schmidt, H. Koskinen, J.U. Kozyra, J.G. Luhmann, E.C. Roelof, D.J. Williams, S. Livi, C.C. Curtis, K.C. Hsieh, B.R. Sandel, M. Grande, M. Carter, J.-A. Sauvaud, A. Fedorov, J.-J. Thocaven, S. McKenna-Lawler, S. Orsini, R. Cerulli-Irelli, M. Maggi, P. Wurz, P. Bochsler, N. Krupp, J. Woch, M. Fränz, K. Asamura, C. Dierker, Icarus **182**(2), 371–382 (2006)

R.A. Frahm, J.R. Sharber, J.D. Winningham, R. Link, M.W. Liemohn, J.U. Kozyra, A.J. Coates, D.R. Linder, S. Barabash, R. Lundin, A. Fedorov, Icarus **206**, 50–63 (2010)

M. Fränz, E. Dubinin, E. Nielsen, J. Woch, S. Barabash, R. Lundin, A. Fedorov, Planet. Space Sci. **58**, 1442–1454 (2010)

G.W. Fraser, J.F. Pearson, J.E. Lees, Nucl. Instrum. Methods Phys. Res. A **254**, 447–462 (1987)

F. González-Galindo, S.W. Bougher, M.A. López-Valverde, F. Forget, J. Murphy, Planet. Space Sci. **58**, 1832–1849 (2010)

R.R. Goruganthu, W.G. Wilson, Rev. Sci. Instrum. **55**(12), 2030–2033 (1984)

D.A. Gurnett, R.L. Huff, D.D. Morgan, A.M. Persoon, T.F. Averkamp, D.L. Kirchner, F. Duru, F. Akalin, A.J. Kopf, E. Nielsen, A. Safaeinili, J.J. Plaut, G. Picardi, Adv. Space Res. **41**, 1335–1346 (2008)

J.S. Halekas, D.A. Brain, R.P. Lin, J.G. Luhmann, D.L. Mitchell, Adv. Space Res. **41**, 1347–1352 (2008)

J.S. Halekas, E.R. Taylor, G. Dalton, G. Johnson, D.W. Curtis, J.P. McFadden, D.L. Mitchell, R.P. Lin, B.M. Jakosky, Space Sci. Rev. **195**(1), 125–151 (2015)

K. Ishisaka, T. Okada, K. Tsuruda, H. Hayakawa, T. Mukai, H. Matsumoto, J. Geophys. Res. **106**, 6309–6320 (2001)

Y. Itikawa, J. Phys. Chem. Ref. Data **31**, 749–767 (2002)

B.M. Jakosky, R.P. Lin, J.M. Grebowsky, J.G. Luhmann, D.F. Mitchell, G. Beutelschies, T. Priser, M. Acuna, L. Andersson, D. Baird, D. Baker, R. Bartlett, M. Benna, S. Bougher, D. Brain, D. Carson, S. Cauffman, P. Chamberlin, J.-Y. Chaufray, O. Cheatom, J. Clarke, J. Connerney, T. Cravens, D. Curtis, G. Delory, S. Demcak, A. DeWolfe, F. Eparvier, R. Ergun, A. Eriksson, J. Espley, X. Fang, D. Folta, J. Fox, C. Gomez-Rosa, S. Habenicht, J. Halekas, G. Holsclaw, M. Houghton, R. Howard, M. Jarosz, N. Jedrich, M. Johnson, W. Kasprzak, M. Kelley, T. King, M. Lankton, D. Larson, F. Leblanc, F. Lefevre, R. Lillis, P. Mahaffy, C. Mazelle, W. McClintock, J. McFadden, D.L. Mitchell, F. Montmessin, J. Morrissey, W. Peterson, W. Possel, J.-A. Sauvaud, N. Schneider, W. Sidney, S. Sparacino, A.I.F. Stewart, R. Tolson, D. Toublanc, C. Waters, T. Woods, R. Yelle, R. Zurek, Space Sci. Rev. **195**(1), 3–48 (2015)

A.M. Krimskii, T.K. Breus, N.F. Ness, D.P. Hinson, D.I. Bojkov, J. Geophys. Res. **108**, 1431 (2003)

D.E. Larson, R.J. Lillis, C.O. Lee, P.A. Dunn, K. Hatch, M. Robinson, D. Glaser, J. Chen, D. Curtis, C. Tiu, R.P. Lin, J.G. Luhmann, B.M. Jakosky, Space Sci. Rev. **195**(1), 153–172 (2015)

M.W. Liemohn, R.A. Frahm, J.D. Winningham, Y. Ma, S. Barabash, R. Lundin, J.U. Kozyra, A.F. Nagy, S.M. Bougher, J. Bell, D. Brain, D. Mitchell, J. Luhmann, M. Holmström, H. Andersson, M. Yamauchi, A. Grigoriev, S. McKenna-Lawler, J.R. Sharber, J.R. Scherrer, S.J. Jeffers, A.J. Coates, D.R. Linder, D.O. Kataria, E. Kallio, H. Koskinen, T. Säles, P. Riiheläh, W. Schmidt, E. Roelof, D. Williams, S. Livi, C.C. Curtis, K.C. Hsiehj, B.R. Sandel, M. Grande, M. Carter, J.-A. Sauvaud, A. Fedorov, J.-J. Thocaven, S. Orsini, R. Cerulli-Irelli, M. Maggi, P. Wurzn, P. Bochsler, N. Kruppo, J. Woch, M. Fränzo, K. Asamurap, C. Dierker, Icarus **182**, 383–395 (2006)

R.J. Lillis, D.L. Mitchell, R.P. Lin, M.H. Acuña, Icarus **194**, 544–561 (2008a)

R.J. Lillis, S.W. Bougher, D.L. Mitchell, D.A. Brain, R.P. Lin, M.H. Acuña, Icarus **194**, 562–574 (2008b)

R.J. Lillis, H. Frey, M. Manga, D.L. Mitchell, R.P. Lin, M.H. Acuña, S.W. Bougher, Icarus **194**, 575–596 (2008c)

R.J. Lillis, M.O. Fillingim, L.M. Peticolas, D.A. Brain, R.P. Lin, S.W. Bougher, J. Geophys. Res. **114**, E11009 (2009). doi:10.1029/2009JE003379

R.J. Lillis, M.O. Fillingim, D.A. Brain, J. Geophys. Res. **116**, A12317 (2011). doi:10.1029/2011JA016982

P.R. Mahaffy, M. Benna, T. King, D.N. Harpold, R. Arvey, M. Barciniak, M. Bendt, D. Carrigan, T. Errigo, V. Holmes, C.S. Johnson, J. Kellogg, P. Kimvilakani, M. Lefavor, J. Hengemihle, F. Jaeger, E. Lyness, J. Maurer, A. Melak, F. Noreiga, M. Noriega, K. Patel, B. Prats, E. Raaen, F. Tan, E. Weidner, C. Gundersen, S. Battel, B.P. Block, K. Arnett, R. Miller, C. Cooper, C. Edmonson, J.T. Nolan, Space Sci. Rev. **195**(1), 49–73 (2015)

W.E. McClintock, N.M. Schneider, G.M. Holsclaw, J.T. Clarke, A.C. Hoskins, I. Stewart, F. Montmessin, R.V. Yelle, J. Deighan, Space Sci. Rev. **195**(1), 75–124 (2015)

J.P. McFadden, in *Calibration of Particle Instruments in Space Physics*, ed. by M. Wüest, D. Evans, R. von Steiger (2007), pp. 409–422. Appendix 1

J.P. McFadden, D.S. Evans, W.T. Kasprzak, L.H. Brace, D.J. Chornay, A.J. Coates, B.K. Dichter, W.R. Hoegy, E. Holeman, K. Kadinsky-Cade, J.C. Kasper, D. Kataria, L. Kistler, D. Larson, A.J. Lazarus, F. Mozer, K.W. Ogilvie, G. Paschmann, Y. Saito, J.D. Scudder, J.T. Steinberg, M. Wüest, P. Wurz, F. Rich, in *Calibration of Particle Instruments in Space Physics*, ed. by M. Wüest, D. Evans, R. von Steiger (2007), pp. 293–408. Ch. 4

J.P. McFadden, C.W. Carlson, D. Larson, M. Ludham, R. Abiad, B. Elliot, P. Turin, M. Marckwordt, V. Angelopoulos, Space Sci. Rev. **141**, 277–302 (2008)

J.P. McFadden, O. Kortmann, D. Curtis, G. Dalton, G. Johnson, R. Abiad, R. Sterling, K. Hatch, P. Berg, C. Tiu, D. Gordon, S. Heavner, M. Robinson, M. Marckwordt, R. Lin, B. Jakosky, Space Sci. Rev. **195**(1), 199–256 (2015)

D.L. Mitchell, R.P. Lin, H. Rème, D.H. Crider, P.A. Cloutier, J.E.P. Connerney, M.H. Acuña, N.F. Ness, Geophys. Res. Lett. **27**(13), 1871–1874 (2000)

D.L. Mitchell, R.P. Lin, C. Mazelle, H. Rème, P.A. Cloutier, J.E.P. Connerney, M.H. Acuña, N.F. Ness, J. Geophys. Res. **106**(E10), 23419–23427 (2001)

D.L. Mitchell, R.J. Lillis, R.P. Lin, J.E.P. Connerney, M.H. Acuña, J. Geophys. Res. **112**, E01002 (2007). doi:10.1029/2005JE002564

F. Němec, D.D. Morgan, D.A. Gurnett, F. Duru, J. Geophys. Res. **115**, E12009 (2010). doi:10.1029/2010JE003663

J.-A. Sauvaud, D. Larson, C. Aoustin, D. Curtis, J.-L. Médale, A. Fedorov, J. Rouzaud, J. Luhmann, T. Moraeu, P. Schröder, P. Louarn, I. Dandouras, E. Penou, Space Sci. Rev. **136**(1–4), 227–239 (2008)

M.B. Shah, D.S. Elliott, H.B. Gilbody, J. Phys. B **20**, 3501 (1987)

O.H.W. Siegmund, J. Vallerga, B. Wargelin, IEEE Trans. Nucl. Sci. **35**, 524–528 (1988)

W.R. Thompson, M.B. Shah, H.B. Gilbody, J. Phys. B **28**, 1321 (1995)

D. Ulusen, D.A. Brain, D.L. Mitchell, J. Geophys. Res. **116**, A07214 (2011). doi:10.1029/2010JA016217
D. Uluşen, I.R. Linscott, J. Geophys. Res. **113**, E06001 (2008). doi:10.1029/2007JE002916
P. Withers, M. Mendillo, D.P. Hinson, K. Cahoy, J. Geophys. Res. **113**, A12314 (2008). doi:10.1029/2008JA013636
M.H.G. Zhang, J.G. Luhmann, A.J. Kliore, J. Geophys. Res. **95**, 17095–17102 (1990)
T. Zurbuchen, P. Bochsler, F. Scholze, Opt. Eng. **34**(5), 1303–1315 (1995)